Research Square

Preprints are preliminary reports that have not undergone peer review.
They should not be considered conclusive, used to inform clinical practice,
or referenced by the media as validated information.

Quantum Chemical Evidence for Localized O1–C5=C4 Reactivity in 2,3-Dihydrofuran

Khakendra Basnet
Tribhuvan University
Jeevan Ghimire
Nepal Academy of Science and Technology
Bhijan Neupane
bhijanneupane@outlook.com

Nepal Academy of Science and Technology

Research Article

Keywords: 2,3-dihydrofuran, DFT, FMO, Fukui function, MEP, NBO, ELF

Posted Date: June 5th, 2026

DOI: https://doi.org/10.21203/rs.3.rs-9698111/v1

License: This work is licensed under a Creative Commons Attribution 4.0 International License.
Read Full License

Additional Declarations: No competing interests reported.

Quantum Chemical Evidence for Localized O1–C5=C4 Reactivity in 2,3-Dihydrofuran

Khakendra Basnet[1, a], Jeevan Ghimire[b], Bhijan Neupane[*, b]

[a]Department of Physics, Patan Multiple Campus, Tribhuvan University, Patandhoka, Lalitpur, 44700, Bagmati, Nepal

[b]Faculty of Technology, Materials Science & Nanotechnology Laboratory, Nepal Academy of Science and Technology, Khumaltar, Lalitpur, Bagmati, Nepal

[*]Corresponding Author: bhijanneupane@outlook.com

Abstract

2,3-Dihydrofuran is a small oxygen-containing heterocycle whose enol-ether unit makes it useful in synthesis, oxidation chemistry, and polymer-related transformations; however, its global electronic stability and local reactive behavior are not always clearly distinguished. Density functional theory calculations were performed at the B3LYP/6-311++G(d,p) level to examine the geometry, frontier orbitals, global reactivity descriptors, local reactivity indices, electrostatic potential, donor–acceptor interactions, weak contacts, and electron localization features of 2,3-dihydrofuran. The optimized neutral structure showed a slightly puckered five-membered ring, indicating the partial release of ring strain while preserving the electronically active O1–C5=C4 enol-ether fragment. The gas-phase highest occupied molecular orbital–lowest unoccupied molecular orbital separation was 5.77 eV, and solvent calculations produced only small changes, indicating that continuum solvation does not strongly modify the frontier orbital pattern. Global descriptors therefore describe 2,3-dihydrofuran as a comparatively hard neutral species; however, molecular electrostatic potential, Fukui function, dual descriptor, and natural bond orbital analyses consistently identify the oxygen atom and C4=C5 unit as the dominant local response regions. The strongest donor–acceptor interaction, LP(2) O1 → π*(C4–C5), with a stabilization energy of 28.6 kcal mol^{-1}, explains the electronic origin of this localized reactivity. Reduced density gradient, electron localization function, and localized orbital locator analyses further revealed weak intraring contacts, steric repulsion, localized σ bonds, and oxygen-assisted delocalization. These combined descriptors show that 2,3-dihydrofuran is globally stable but locally activated at the O1–C5=C4 region, providing atom-level guidance for reaction site selection and mechanistic modeling.

Keywords: 2,3-dihydrofuran; DFT; FMO; Fukui function; MEP; NBO; ELF

Introduction

2,3-Dihydrofuran (2,3-DHF) is a five-membered oxygen-containing heterocycle reported in plant-related chemical profiles and is widely recognized as a reactive enol-ether motif [1,2]. Its structural identity is defined by a C=C bond adjacent to an ether oxygen, which distinguishes it from fully saturated tetrahydrofuran, aromatic furan, and other dihydrofuran isomers. This structural difference is chemically important because the oxygen lone pairs can interact with neighboring unsaturated bonds. This produces a localized O-C=C electronic domain that influences electrophilic addition, radical activation, oxidation, ring opening, and polymerization behavior [3-8].

Recent studies show 2,3-DHF and related furan derivatives are relevant in polymer chemistry, oxidation, photochemistry, radical chemistry, catalysis, kinetic modeling, and synthetic methodology. An et al. (2023) used 2,3-DHF in living alternating ring-opening metathesis copolymerization, producing degradable polymers and highlighting its value in sustainable polymer synthesis [9]. In oxidation chemistry, Alwe et al. (2015) investigated hydroxyl-radical-initiated oxidation of 2,3-DHF and 2,5-dihydrofuran, showing unsaturation position affects the oxidation pathway [10]. Matsubara et al. (2016) showed infrared free-electron-laser excitation can induce isomerization and dissociation of 2,3-DHF, indicating vibrational excitation may promote structural rearrangement and bond cleavage [11]. Radical reactivity was examined by Mozafari et al. (2016), who characterized radicals from furan, 2,3-DHF, and 2,5-dihydrofuran, linking the dihydrofuran framework with radiation- or particle-induced radical formation [12]. The synthetic and catalytic importance of this framework was reported in related studies. Guðmundsson et al. (2018) described iron-catalyzed cycloisomerization of α-allenols as an efficient route to 2,3-DHF, supporting this scaffold's role in catalytic reaction design [13]. Wu et al. (2020) measured ignition delay times and modeled low- to intermediate-temperature oxidation behavior of furan, 2,3-DHF, and tetrahydrofuran, showing ring saturation and double-bond position influence combustion reactivity [14]. In related furan chemistry, Salnikov et al. (2018) used parahydrogen-assisted methods to examine heterogeneous hydrogenation of furan derivatives [15], while Schalk et al. (2018) investigated ring-opening channels and Rydberg states' influence on furan and its derivatives' excited-state dynamics [16]. Kanhounnon et al. (2019) applied quantum-mechanical modeling to furan and 2-methylfuran hydrodeoxygenation on metal sulfide clusters, showing the importance of oxygen-containing furan frameworks in catalytic deoxygenation processes [17]. Electronic and synthetic studies of related systems support a detailed molecular-level interpretation of 2,3-DHF. Röder et al. (2020) reported high-resolution vacuum-ultraviolet absorption spectra of 2,3- and 2,5-dihydrofuran, providing useful information for understanding their excited-state behavior [18]. Guerra Faura et al. (2021) showed catalyst-controlled chemodivergent reactions of enol ethers can produce 1,2-dihydrofuran acetals and substituted indoles, emphasizing unsaturated oxygen-containing rings' synthetic flexibility [19]. Choi and Hong (2023) developed chemically recyclable oxygen-protective polymers through ring-opening metathesis polymerization of cyclohexene derivatives, placing oxygen-containing cyclic olefins in recyclable polymer design [20]. Together, these reports establish 2,3-DHF and related furan systems' broad chemical relevance. However, most focus on specific reactions, substituted derivatives, kinetic behavior, or broader furan chemistry. A connected description is needed to explain how parent 2,3-DHF's electronic stability coexists with localized reactivity in the O1–C5=C4 enol-ether region.

This unresolved point is important because a molecule can exhibit a comparatively large HOMO-LUMO gap and still contain a localized reactive fragment. For 2,3-DHF, the key question is how the global electronic hardness coexists with the known reactivity of the oxygen-adjacent C=C bond. Therefore, a combined quantum-chemical interpretation is needed to relate frontier orbital behavior, global reactivity parameters, molecular electrostatic potential, Fukui-function response, donor-acceptor interactions, and real-space electron density descriptors to the same reactive region.

The present study addresses this question by examining the optimized geometry, frontier molecular orbitals in the gas phase and selected solvents, global reactivity descriptors from density functional theory, Fukui functions, dual descriptors, molecular electrostatic potential, natural bond orbital interactions, and real-space electron density features at the B3LYP/6-311++G(d,p) level. The aim was to identify the atom and bond regions most relevant to reactivity, explain the electronic origin of the O1–C5=C4 response, and provide practical descriptors for reaction site selection, mechanistic modeling, and comparison with substituted oxygen-containing heterocycles.

Methodology

All quantum chemical calculations were performed using Gaussian 09 W, and the molecular structures and selected outputs were visualized using GaussView [21,22]. Geometry optimization and electronic structure calculations were performed using density functional theory (DFT), which solves the Kohn-Sham equations to obtain the ground-state electron density and related molecular properties [23,24]. The Becke three-parameter Lee-Yang-Parr (B3LYP) hybrid exchange-correlation functional was selected because it is widely used for small organic molecules and provides a practical balance between accuracy and computational cost [25-27]. The 6-311++G(d,p) basis set, which includes diffuse and polarization functions, was used to consistently describe the valence and weakly bound electron densities.

To account for medium effects, a solvation model based on density (SMD) was used for dimethyl sulfoxide (DMSO), chloroform, and diethyl ether [28]. SMD was chosen because it is a broadly applicable continuum model that efficiently incorporates solvent polarization into quantum-chemical calculations. All solvent-phase properties were computed using the same functional/basis set to allow consistent comparisons across media. Frontier molecular orbital (FMO) energies, including the highest occupied molecular orbital (HOMO) and lowest unoccupied molecular orbital (LUMO), were extracted to discuss electronic stability and estimate conceptual DFT descriptors. The global reactivity parameters (GRPs) were calculated using standard DFT equations [29,30]. The ionization potential (I) and electron affinity (A) were approximated from the frontier orbital energies using a Koopmans-type estimate.

For the cationic radical species, calculations were performed using an unrestricted, open-shell formalism. The α- and β-spin orbital manifolds were analyzed as the spin components of the same open-shell cation rather than as two separate cationic species. The expectation value $\langle S^2 \rangle$ was checked to evaluate possible spin contamination and support the reliability of the unrestricted calculation. Natural bond orbital (NBO) analysis was performed to interpret the electronic structure in terms of Lewis and non-Lewis contributions, donor-acceptor interactions, and hyperconjugation [31]. Second-order perturbation analysis was used to quantify the donor-acceptor stabilization energies based on the interactions between filled donor NBOs and vacant acceptor NBOs [32]. Higher second-order perturbation stabilization energy E(2) values indicate stronger delocalization or hyperconjugative stabilization and more pronounced donor-acceptor coupling within the molecule [33]. For the nonlinear optical (NLO) analysis, the molecular response to an applied electric field was evaluated using the total dipole moment (μ_{tot}), mean polarizability (α), polarizability anisotropy ($\Delta\alpha$), and first-order hyperpolarizability (β_{tot}), which were all calculated at the same density functional theory level. These parameters describe the field-induced polarization behavior of the molecule and provide theoretical descriptors for assessing its possible NLO response [34]. The electronic excitation energies and corresponding transitions were calculated using time-dependent density functional theory (TD-DFT) at the B3LYP/6-311++G(d,p) level of theory. The ultraviolet-visible (UV-vis) absorption behavior was discussed using the Beer-Lambert relationship between absorbance and concentration/path length [35,36]. Local reactivity was assessed using Fukui functions, dual descriptors, and atom-wise natural population analysis (NPA) charge-difference values at optimized neutral geometries [37,38]. Wavefunction-based analyses, including density of states (DOS) where applicable, electrostatic potential, reduced density gradient (RDG), electron localization function (ELF), and localized orbital locator (LOL), were performed using Multiwfn and visualized using Visual Molecular Dynamics (VMD) software [39,40]. The RDG analysis was used to reveal weak interaction regions from the electron density and its gradient [41]. The interaction types were interpreted using the $\mathrm{sign}(\lambda_2)\rho$, where negative values correspond to attractive interactions, values near zero indicate weak van der Waals contacts, and positive values indicate repulsive or steric regions [41]. Electron localization was further characterized using the electron localization function (ELF) and localized orbital locator (LOL) to visualize the localized and delocalized bonding features [42-45].

Results and Discussion

Geometrical Optimization

Geometry optimization was performed first because all subsequent electronic and reactivity descriptors depended on the equilibrium structure. The equilibrium geometry of 2,3-DHF was optimized at the B3LYP/6-311++G(d,p) level of theory using Gaussian 09 W. The optimization minimized the electronic energy with respect to the atomic coordinates, and the optimized structure was used for subsequent electronic structure and reactivity analyses [46].

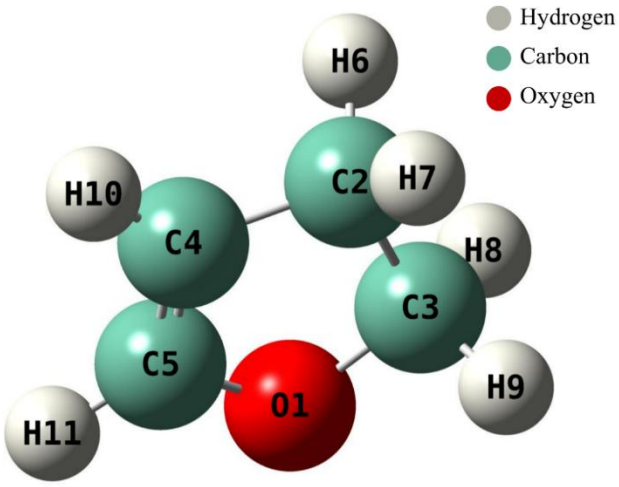


Figure 1. Optimized structure of 2,3-DHF.

The optimized neutral singlet structure is presented in Figure 1. 2,3-DHF contains 11 atoms and 38 electrons and was treated as a closed-shell neutral species.

The selected geometrical parameters in Table 1 were examined to understand the ring strain, bond unsaturation, and conformational changes after ionization. In the gas phase, the calculated bond lengths ranged from 1.0752 Å for C5-H11 to 1.5268 Å for C2-C3. In the cationic state, the corresponding range was 1.0791 Å for C4-H10 to 1.5464 Å for C2-C3. The C4-C5 distance of 1.3265 Å in the neutral singlet form is consistent with the unsaturated enol-ether fragment, whereas the longer C2-C3 distance is characteristic of a single bond. The bond angle range of approximately 101-128° reflects the constrained five-membered ring geometry and the influence of the oxygen lone pairs [47-50]. Torsion angles close to ±180°and small deviations around the O-C-C-C framework indicate a slightly puckered, nonplanar ring conformation, which helps reduce ring strain and influences the spatial orientation of the reactive C=C unit [51].

Table 1. Calculated bond lengths (Å), bond angles (°), and torsion angles (°) for 2,3-DHF.

Atoms	Bond length (Å)		Atoms	Bond angle (°)		Atoms	Torsion angles (°)	
	Gas phase	Cation		Gas phase	Cation		Gas phase	Cation
O1-C3	1.4427	1.4566	C3-O1-C5	103.5656	106.5007	C5-O1-C3-C2	-11.2353	-13.1469
O1-C5	1.3767	1.3676	C3-C2-C4	101.3086	101.117	C5-O1-C3-H8	-133.213	-136.016
C2-C3	1.5268	1.5464	C3-C2-H6	111.4694	112.2208	C5-O1-C3-H9	109.5184	106.6796

C2-C4	1.477	1.5148	C3-C2-H7	111.4628	111.5408	C3-O1-C5-C4	6.9031	7.404
C2-H6	1.0945	1.0967	C4-C2-H6	110.9827	111.4843	C3-O1-C5-H11	-174.585	-173.477
C2-H7	1.0937	1.0934	C4-C2-H7	112.8264	113.3374	C4-C2-C3-O1	11.4284	13.5563
C3-H8	1.0952	1.0897	H6-C2-H7	108.6961	107.2061	C4-C2-C3-H8	131.7828	132.1538
C3-H9	1.0965	1.0938	O1-C3-C2	108.7757	106.5295	C4-C2-C3-H9	-107.444	-103.277
C4-C5	1.3265	1.3314	O1-C3-H8	109.0163	107.5659	H6-C2-C3-O1	-106.674	-105.356
C4-H10	1.0786	1.0791	O1-C3-H9	108.0899	107.2324	H6-C2-C3-H8	13.6802	13.2417
C5-H11	1.0752	1.0808	C2-C3-H8	111.6644	114.2151	H6-C2-C3-H9	134.4534	137.8107
			C2-C3-H9	111.1165	111.7854	H7-C2-C3-O1	131.6749	134.3268
			H8-C3-H9	108.0937	109.1651	H7-C2-C3-H8	-107.971	-107.076
			C2-C4-C5	108.4249	108.5787	H7-C2-C3-H9	12.8026	17.4932
			C2-C4-H10	125.8124	125.5309	C3-C2-C4-C5	-7.2745	-9.5704
			C5-C4-H10	125.7313	125.7962	C3-C2-C4-H10	174.6717	173.7981
			O1-C5-C4	116.5457	115.3041	H6-C2-C4-C5	111.1796	109.8706
			O1-C5-H11	115.0323	114.6068	H6-C2-C4-H10	-66.8742	-66.7608
			C4-C5-H11	128.402	130.0818	H7-C2-C4-C5	-126.551	-129.063
						H7-C2-C4-H10	55.3957	54.3059
						C2-C4-C5-O1	0.5586	1.884
						C2-C4-C5-H11	-177.721	-177.07
						H10-C4-C5-O1	178.6144	178.5042
						H10-C4-C5-H11	0.3346	-0.4494

HOMO-LUMO Gap Analysis

Frontier molecular orbital (FMO) analysis was used to evaluate the electron-donating and electron-accepting tendencies of 2,3-DHF. In this analysis, the highest occupied molecular orbital (HOMO) indicates the region and energy level most relevant to electron donation, whereas the lowest unoccupied molecular orbital (LUMO) indicates the region and energy level most relevant to electron acceptance [52]. The calculated HOMO and LUMO energies of the neutral singlet structure in the gas phase were -5.98349 and -0.21024 eV, respectively, giving a HOMO-LUMO separation of 5.77326 eV, as shown in Figure 2.

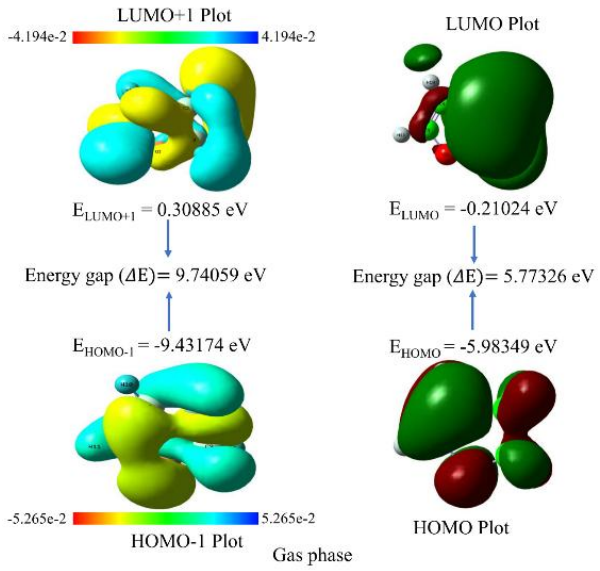


Figure 2. Molecular orbitals and energies of 2,3-DHF in the gas phase.

The calculated HOMO-LUMO separation indicates a relatively large electronic gap for the isolated neutral singlet form at the DFT level. This supports a comparatively hard electronic structure; however, it does not imply that 2,3-DHF is chemically inert under all reaction conditions. The HOMO-1 and LUMO+1 energies were -9.43174 and 0.30885 eV, respectively, resulting in a HOMO-1-LUMO+1 separation of 9.74059 eV. SMD solvent calculations yielded slightly larger HOMO-LUMO gaps of 5.86839 eV in DMSO, 5.86404 eV in chloroform, and 5.83839 eV in diethyl ether, as shown in Figure 3(a-e). These small solvent-dependent changes suggest that continuum solvation modestly perturbs the frontier orbital energies while preserving the same overall electronic pattern [53,54].

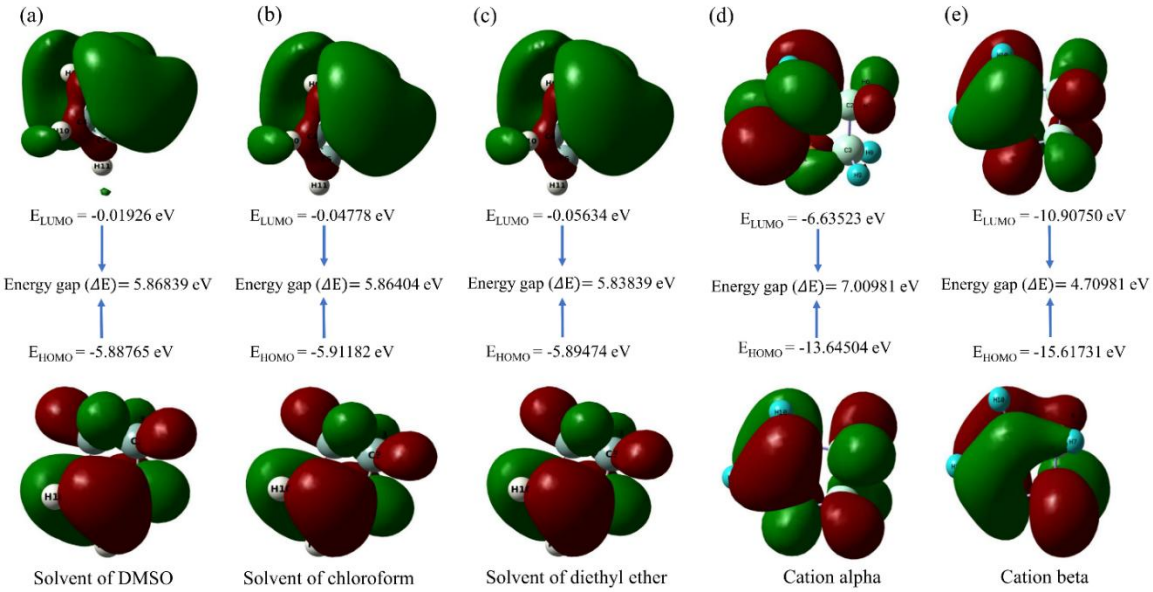


Figure 3. HOMO and LUMO energies of 2,3-DHF in (a) DMSO, (b) chloroform, (c) diethyl ether, and the open-shell cationic state represented by (d) alpha-spin, and (e) beta-spin orbital manifolds.

For the open-shell cation, Figure 3(d,e) show the alpha- and beta-spin orbital manifolds calculated at the B3LYP/6-311++G(d,p) level. This spin-resolved analysis was included to show how electron removal changes the orbital distribution. The alpha-spin and beta-spin HOMO-LUMO separations are 7.00981 and 4.70981 eV, respectively. These values describe the spin-dependent orbital structure of a single cationic species and should not be interpreted as two independent cationic molecules. Because conceptual DFT descriptors derived from frontier orbital energies are the most reliable for comparable electronic states, the cationic columns were retained only as qualitative spin-resolved orbital descriptors. The quantitative use of the open-shell cation would require reporting the calculated <S2> value. This validated the ionization and electron affinity trends through delta self-consistent field calculations [55,56].

Global Reactivity Parameter (GRP) Calculations

Global reactivity parameter (GRP) analysis was performed to convert the frontier orbital energies into whole molecule descriptors. The GRPs calculated at the B3LYP/6-311++G(d,p) level are summarized in Table 2 [57-59]. These descriptors complement the FMO analysis by indicating the overall resistance of 2,3-DHF to the charge transfer. The gas-phase hardness of 2.88662 eV and softness of 0.34643 eV^{-1} indicate a relatively hard neutral singlet form within the Koopmans-type approximation. Simultaneously, the enol ether C=C fragment and oxygen lone pairs remain chemically important local features. The negative

chemical potential indicates a tendency to retain electron density, whereas the moderate electrophilicity index indicates a limited but non-negligible electron-accepting capacity [60].

Table 2. Calculated electronic energies and global reactivity parameters of 2,3-DHF at the B3LYP/6-311++G(d,p) level of theory.

Global reactivity Parameters	Gas Phase	DMSO	Chloroform	Diethyl ether	Cation α-spin	Cation β-spin
EHOMO (eV)	-5.98349 eV	-5.88765 eV	-5.91182 eV	-5.89474 eV	-13.64504 eV	-15.61731 eV
ELUMO (eV)	-0.21024 eV	-0.01926 eV	-0.04778 eV	-0.05634 eV	-6.63523 eV	-10.90750 eV
Energy gap ΔE(ELUMO-EHOMO)	5.77326 eV	5.86839 eV	5.86404 eV	5.83839 eV	7.00981 eV	4.70981 eV
Ionization energy (I)	5.98349 eV	5.88765 eV	5.91182 eV	5.89474 eV	13.64504 eV	15.61731 eV
Electron affinity (A)	0.21024 eV	0.01926 eV	0.04778 eV	0.05634 eV	6.63523 eV	10.90750 eV
Chemical hardness (η)	2.88662 eV	2.93419 eV	2.93202 eV	2.91920 eV	3.50490 eV	2.35490 eV
Chemical softness (S)	0.34643 eV^{-1}	0.34081 eV^{-1}	0.34106 eV^{-1}	0.34256 eV^{-1}	0.28531 eV^{-1}	0.42465 eV^{-1}
Nucleofugality (ΔEn)	0.00766 eV	0.00006 eV	0.00039 eV	0.00054 eV	6.28067 eV	25.26080 eV
Global electrophilicity index (ω)	1.66121 eV	1.48642 eV	1.51418 eV	1.51648 eV	14.66835 eV	37.34575 eV
Electronegativity (χ)	3.09686 eV	2.95345 eV	2.97980 eV	2.97554 eV	10.14014 eV	13.26241 eV
Chemical potential (μ)	-3.09686 eV	-2.95345 eV	-2.97980 eV	-2.97554 eV	-10.14014 eV	-13.26241 eV
Electrofugality (ΔEe)	6.20139 eV	5.90697 eV	5.95999 eV	5.95162 eV	26.56094 eV	51.78561 eV

In the neutral gas phase, the electrophilicity index, electronegativity is 3.09686 eV, and chemical potential were 1.66121, 3.09686, and -3.09686 eV, respectively. In the SMD solvent calculations, the HOMO-LUMO gaps and hardness values changed only slightly, with DMSO, chloroform, and diethyl ether showing similar trends. These results indicate that the continuum solvent effects do not qualitatively alter the electronic hardness of the molecule. The cationic α- and β-spin columns in Table 2 represent the orbital manifolds of the same open-shell cation, not two separate cationic forms. Therefore, the cationic α- and β-spin values are retained only for a qualitative discussion of the spin-resolved orbital structure of the radical cation. A direct comparison with the neutral closed-shell descriptors should be avoided because the two systems have different charges and spin states [61,62].

Natural Bond Orbital (NBO) Analysis

Natural bond orbital (NBO) analysis was used to identify the donor-acceptor interactions responsible for electron delocalization in 2,3-DHF. This analysis converts the delocalized wavefunction into localized bonding, antibonding, and lone pair orbitals. This allowed the electronic origin of the reactive O-C=C region to be described in a chemically intuitive manner. Second-order perturbation analysis of the Fock matrix was used to quantify the interactions between the occupied donor NBOs and vacant acceptor NBOs. The stabilization energy E(2) measures the energetic importance of electron delocalization from the donor to the acceptor orbitals [63]. The analysis was performed at the B3LYP/6-311++G(d,p) level to examine the charge delocalization and intramolecular hyperconjugative effects. The key interactions are summarized in Table 3.

Table 3. NBO analysis calculated based on the B3LYP/6-311++G(d,p) method

Donor NBO (i)	Acceptor NBO (j)	Interaction Type	E (2) kcal/mol	E(j)-E(i) a.u.	F(i,j) a.u.

σ (O1-C3)	σ* (C5-H11)	σ → σ*	2.66	1.23	0.051
σ (O1-C5)	σ* (C4-H10)	σ → σ*	2.2	1.31	0.048
σ (C2-C3)	σ* (C4-H10)	σ → σ*	4.42	1.07	0.061
σ (C2-C4)	σ* (O1-C3)	σ → σ*	2.06	0.9	0.038
σ (C2-C4)	σ* (C5-H11)	σ → σ*	5.18	1.07	0.067
σ (C2-H6)	π* (C4-C5)	σ → π*	3.52	0.54	0.04
σ (C2-H7)	π*(C4-C5)	σ → π*	2.65	0.55	0.035
σ C4-C5	σ* (C5-H11)	σ → σ*	2.01	1.19	0.044
π (C4-C5)	σ* (C2-H6)	π → σ*	4.43	0.68	0.049
π (C4-C5)	σ* (C2-H7)	π → σ*	3.93	0.68	0.046
σ (C4-H10)	σ* (O1-C5)	σ → σ*	4.45	0.89	0.056
σ (C5-H11)	σ* (O1-C3)	σ → σ*	2.59	0.82	0.041
CR (1) C5	RY*(3) C4	CR → RY*	2.03	11.25	0.135
LP (1) O1	RY*(1) C3	LP → RY*	2.74	1.54	0.058
LP (1) O1	RY*(1) C5	LP → RY*	3.95	1.58	0.071
LP (1) O1	σ* (C2-C3)	LP → σ*	2.42	0.96	0.043
LP (1) O1	σ* (C4-C5)	LP → σ*	3.21	1.25	0.057
LP (2) O1	RY*(3) C5	LP → RY*	2.06	1.87	0.058
LP (2) O1	σ* (C3-H8)	LP → σ*	3.51	0.7	0.046
LP (2) O1	σ* (C3-H9)	LP → σ*	5.76	0.7	0.058
LP (2) O1	π* (C4-C5)	LP → π*	28.6	0.35	0.089

The strongest donor–acceptor interaction is LP(2) O1 → π*(C4–C5), with a second-order perturbation stabilization energy of 28.6 kcal mol^{-1}. This oxygen lone-pair donation into the antibonding orbital of the C4=C5 bond indicates strong electronic communication within the enol ether fragment. Consequently, the O–C4=C5 region became the principal electronically activated region of 2,3-DHF. Mechanistically, this interaction enhances electron delocalization across the O–C=C fragment and polarizes the double bond, making this region important for electrophilic addition, oxidative or radical activation, and polymerization transformations. Weaker σ(C2–H6) → π(C4–C5) and σ(C2–H7) → π*(C4–C5) interactions, with stabilization energies of 3.52 and 2.65 kcal mol^{-1}, respectively, indicate additional hyperconjugative support from the adjacent C–H bonds [64–66]. Thus, the NBO results show that the stabilization of 2,3-DHF mainly arises from dominant lone-pair (LP)-to-π* donation, weaker σ-to-π* hyperconjugation, and minor σ-to-σ* delocalization. This explains how the molecule can have a relatively large global electronic gap while retaining a localized reactive enol-ether domain.

Nonlinear Optical (NLO) Properties

The nonlinear optical (NLO) properties were evaluated to describe the response of the electron density of 2, 3-DHF to an external electric field. The calculated descriptors include the total dipole moment (μ_{tot}), mean polarizability (⟨α⟩), polarizability anisotropy (Δα), and first-order hyperpolarizability (β_{tot}) at the B3LYP/6-311++G(d,p) level of theory [67]. Equations 1-4 were used to calculate the NLO parameters.

$$\mu_{\text{tot}} = \left(\mu_x^2+\mu_y^2+\mu_z^2\right)^{1/2} \quad (1)$$

$$\langle\alpha\rangle = \frac{\alpha_{xx} + \alpha_{yy} + \alpha_{zz}}{3} \quad (2)$$

$$\Delta\alpha = \frac{1}{\sqrt{2}}\left[(\alpha_{xx} - \alpha_{yy})^2 + (\alpha_{yy} - \alpha_{zz})^2 + (\alpha_{zz} - \alpha_{xx})^2 + 6(\alpha_{xy}^2 + \alpha_{xz}^2 + \alpha_{yz}^2)\right]^{1/2} \quad (3)$$

$$\beta_{\text{tot}} = \left[(\beta_{xxx} + \beta_{xyy} + \beta_{xzz})^2 + (\beta_{yyy} + \beta_{yxx} + \beta_{yzz})^2 + (\beta_{zzz} + \beta_{zxx} + \beta_{zyy})^2\right]^{1/2} \quad (4)$$

Table 4. Nonlinear optical properties calculated based on the B3LYP/6-311++G(d,p) method

Parameters	Value
βxxx	-4.71058
βyyy	9.98603
βzzz	-30.02528
βxyy	88.53046
βxxy	0.59557
βxxz	-3.09965
βxzz	7.72551
βyzz	-15.35937
βyyz	48.70944
βxyz	63.07772
βx (a.u.)	91.54539
βy (a.u.)	-4.77777
βz (a.u.)	15.58452
βtot (a.u.)	92.98528
βtot (esu)	8.03328×10^{-31}
αxx	53.22016
αyy	54.24494
αzz	39.49618
αxy	1.66232
αxz	-0.24155
αyz	-0.17563
α (e.s.u.)	7.25914×10^{-24}
Δα (e.s.u.)	2.15770×10^{-24}
μx (D)	0.33489
μy (D)	0.41947
μz (D)	0.04187
μ (D)	0.53838

Table 4 lists the calculated dipole moments, mean polarizabilities, polarizability anisotropies, and first-order hyperpolarizabilities. Gaussian outputs polarizability and hyperpolarizability in atomic units were converted to electrostatic units using 1 a.u. of $\alpha = 0.1482 \times 10^{-24}$ esu and 1 a.u. of $\beta = 8.6393 \times 10^{-33}$ esu [68]. The total dipole moment was 0.53838 D, with the largest component along the y-axis. The mean polarizability was 7.25914×10^{-24} esu, and the polarizability anisotropy was 2.15770×10^{-24} esu. The calculated first-order hyperpolarizability, β_{tot}, was 92.98528 a.u., corresponding to 8.03328×10^{-31} esu. This value indicates a finite molecular response to an external electric field; however, without comparison to a standard reference molecule or experimental validation, it should be described as a theoretical field-response parameter rather than as evidence that 2,3-DHF is a strong NLO material [69,70].

Ultraviolet-Visible (UV-Vis) Spectra Analysis

Ultraviolet-visible (UV-vis) absorption analysis was performed to examine the low-energy electronic transitions predicted for 2,3-DHF. The transitions were calculated using time-dependent density functional theory (TD-DFT) at the B3LYP/6-311++G(d,p) level, and the solvent effects for DMSO, chloroform, and diethyl ether were included using the SMD continuum model [71]. The calculated absorption maxima are presented in Figure 4. The gas-phase absorption maximum (λ_{max}) was 250.98 nm, whereas the calculated λ_{max} values in dimethyl sulfoxide, diethyl ether, and chloroform were 247.88, 248.90, and 247.86 nm, respectively. The corresponding oscillator strengths (f) were 0.00841, 0.01431, 0.00716, and 0.01295, respectively. The slight decrease in λ_{max} in the solvent phase calculations indicates a small hypsochromic shift, suggesting that the continuum solvent model only weakly perturbs the dominant electronic transition [72]. The n → π* assignment should be considered tentative unless it is supported by tabulated orbital-transition contributions. Nevertheless, the nearly unchanged λ_{max} values indicate that the principal electronic excitation is not strongly affected by solvent polarity [73].

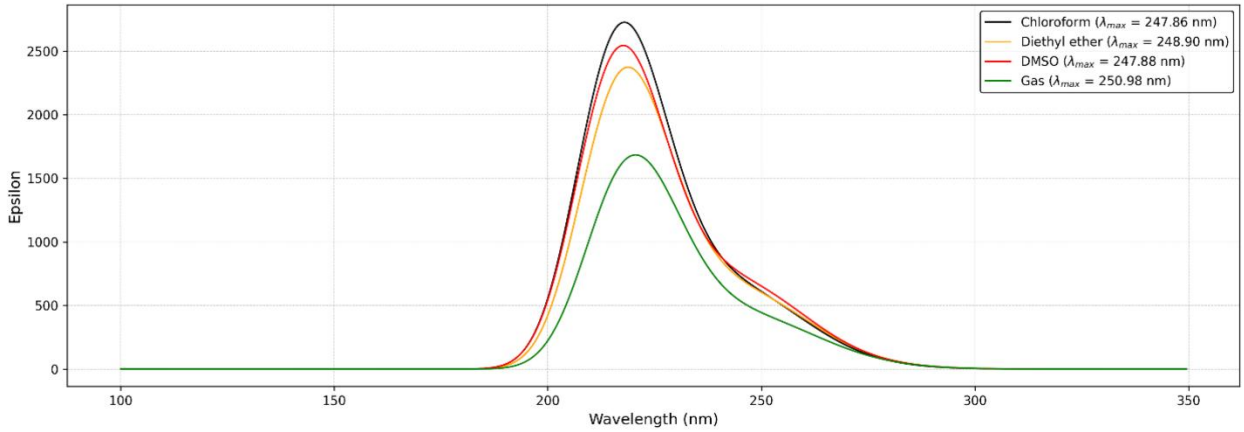


Figure 4. UV-vis spectra of 2,3-DHF in the gas phase, DMSO, diethyl ether, and chloroform.

Density of States (DOS) Analysis

Density of states (DoS) analysis was used to visualize the distribution of the calculated molecular orbital levels across the selected energy range. For isolated molecules, the DoS should be interpreted as a broadened molecular orbital energy distribution rather than a solid-state band structure. The DOS representation was generated using GaussSum 3.0. Figure 5(a) shows the gas-phase DoS from -15 to +15 eV, and Figures 5(b-d) show the corresponding solvent-phase profiles from -20 to +15 eV [74]. The neutral gas-phase HOMO-LUMO separation obtained from the DoS representation was 5.77326 eV, which matched the FMO analysis. The solvent-phase separations of 5.86839, 5.86404, and 5.83839 eV for DMSO, chloroform, and diethyl ether, respectively, confirm that the solvent model slightly shifts the orbital energies but does not change the overall electronic pattern [75,76].

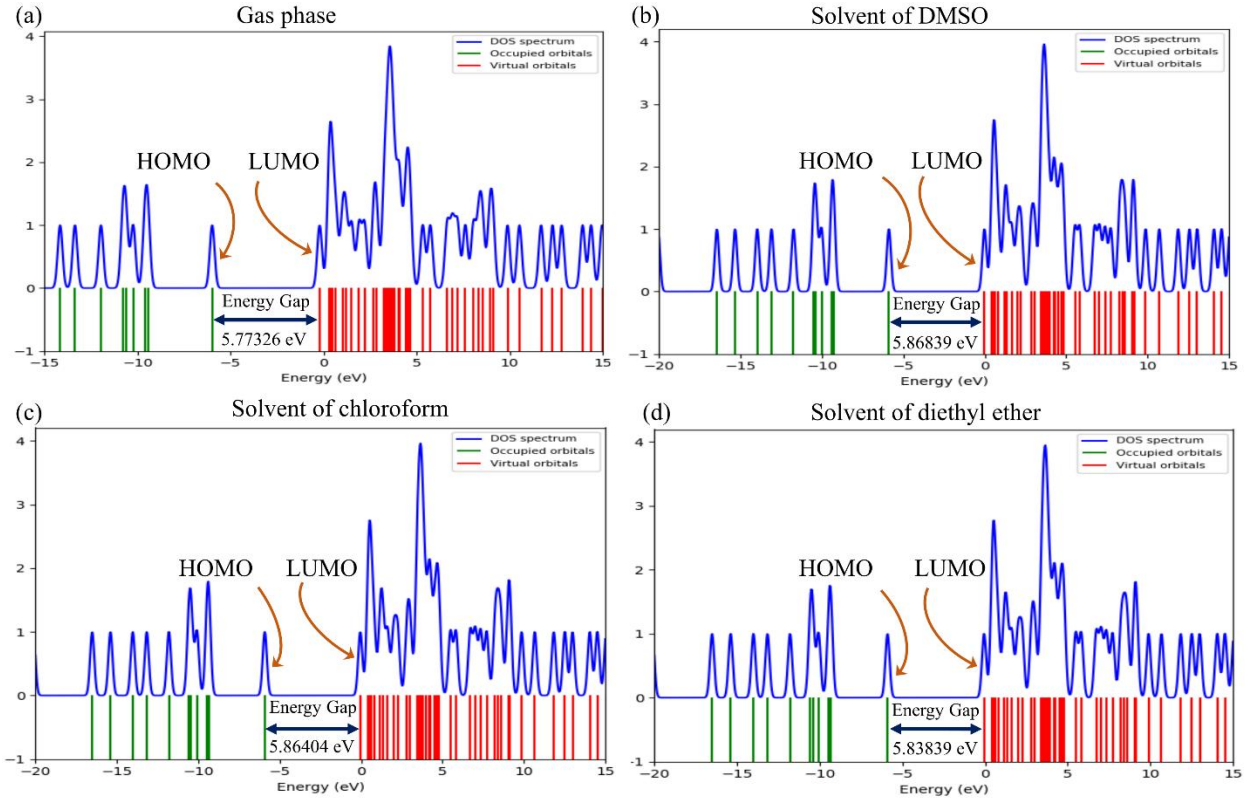


Figure 5. Density of states (DOS) profiles of 2,3-DHF in (a) the gas phase, (b) DMSO, (c) chloroform, and (d) diethyl ether.

The DoS spectrum of the cationic state illustrates how electron removal modifies the distribution of the molecular orbital energies. Figure 6 shows the alpha- and beta-spin DoS profiles over the range of -15 to +15 eV. The peaks indicate clusters of molecular orbital levels, whereas the low-intensity regions indicate fewer available orbital levels in that energy range. The spin-resolved DoS is consistent with the open-shell FMO analysis and helps distinguish the occupied and unoccupied regions of the cationic orbital manifold [77-79].

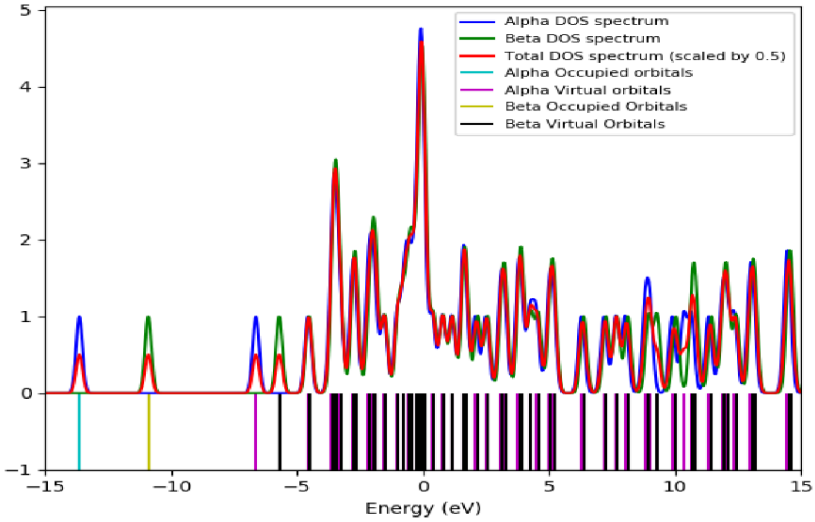


Figure 6. DoS spectra of 2,3-DHF in the cationic state.

Molecular Electrostatic Potential (MEP)

Molecular electrostatic potential (MEP) analysis was performed to locate electron-rich and electron-deficient regions on the molecular surface. This analysis is useful because it links the calculated electron density to the likely electrostatic interactions with electrophiles, nucleophiles, or polar environments. The MEP and contour maps are presented in Figure 7. The map was generated using GaussView from the B3LYP/6-311++G(d,p) electron density data. In the conventional MEP interpretation used here, the red/orange regions represent more negative electrostatic potentials and electron-rich areas, whereas the blue regions represent more positive electrostatic potentials and electron-deficient areas.

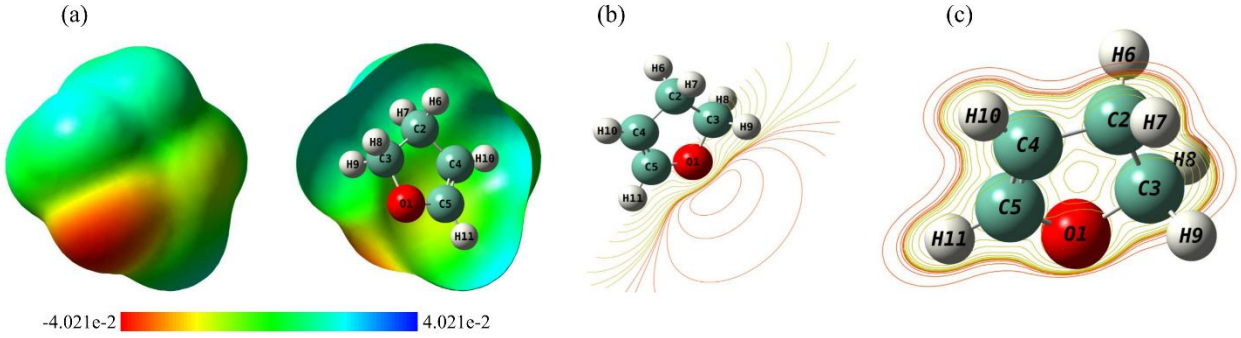


Figure 7. MEP surface map of 2,3-DHF: (a) solid view, (b) gas-phase contour map, and (c) cationic-state contour map.

The neutral singlet structure showed an electrostatic-potential range of approximately -4.021×10^{-2} to $+4.021 \times 10^{-2}$ a.u. on the mapped surface. The negative electrostatic potential is concentrated mainly around the oxygen atom and the electron-rich unsaturated region, indicating sites favorable for interaction with electrophilic species. In contrast, the positive electrostatic potential was localized near the peripheral hydrogen atoms, indicating regions that are more favorable for interaction with nucleophilic species. These molecular electrostatic potential features are consistent with local reactivity analysis; however, they do not independently demonstrate biological activity, which requires separate experimental or target-based evidence [80,81].

Molecular Properties Analysis

Reduced Density Gradient (RDG) Analysis and Its Implications

Reduced density gradient (RDG) analysis was used to visualize weak intramolecular contacts and steric effects from the calculated electron densities. This analysis was included because weak intramolecular contacts and repulsive regions can help explain ring puckering and local conformational preferences. In 2,3-DHF, the relevant interaction types are mainly weak van der Waals contacts within the folded ring framework and steric repulsion arising from close intraring electron-density overlap. Classical intramolecular hydrogen bonding is not expected because the molecule lacks a conventional hydrogen bond donor [82].

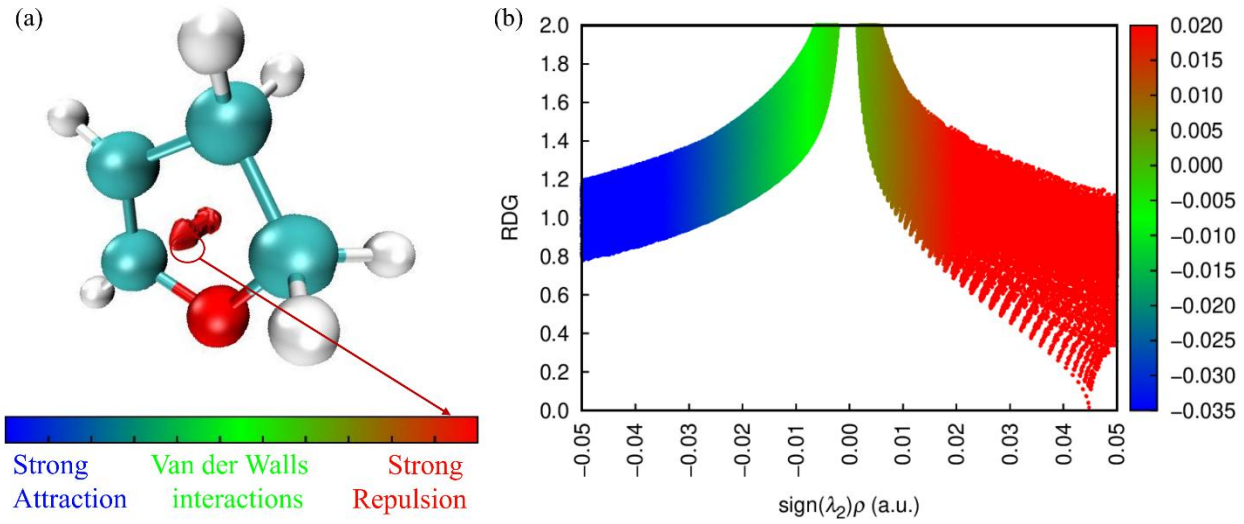


Figure 8. (a) Non-covalent interaction (NCI) surface and (b) RDG plot.

Figure 8 shows the three-dimensional non-covalent interaction (NCI) isosurface and the reduced density gradient (RDG) scatter plot against sign(λ_2)ρ. In this representation, blue regions indicate attractive interactions, green regions indicate weak van der Waals contacts, and red regions indicate steric repulsion [83]. For 2,3-DHF, the main NCI features are green weak-contact regions around the ring framework and red regions associated with steric repulsion from close intraring contacts. These features support the slightly puckered geometry obtained after optimization, as ring puckering helps reduce unfavorable intramolecular crowding while maintaining electronic communication within the O1–C5=C4 enol-ether fragment [84].

Fukui Functions and Dual Descriptors Analysis

The Fukui function and dual descriptor were used to identify the regions of 2,3-DHF that responded most strongly to electron addition or removal. The dual descriptor, $\Delta f(r) = f^{+}(r) - f^{-}(r)$, compares the electron-accepting response function $f^{+}(r)$ with the electron-donating response function $f^{-}(r)$ at the same position in space [85]. Positive $\Delta f(r)$ values indicate regions that are more susceptible to nucleophilic attack, whereas negative $\Delta f(r)$ values indicate regions that are more susceptible to electrophilic attack. In this study, the values and maps were comparatively interpreted to locate the dominant reactive domain of 2,3-DHF.

Table 5. Fukui-function descriptors and dual descriptor values calculated from natural population analysis (NPA).

Atoms	Anion (N+1)	Neutral (N)	Cation (N-1)	$f^{+}(r)$	$f^{-}(r)$	$f^{0}(r)$	$\Delta f(r)$
O1	-0.58155	-0.55374	-0.29983	-0.02781	-0.25391	-0.14086	0.22610
C2	-0.47284	-0.43549	-0.48617	-0.03735	0.05068	0.00667	-0.08803
C3	-0.05315	-0.02227	-0.05523	-0.03088	0.03296	0.00104	-0.06384
C4	-0.32928	-0.30885	-0.00002	-0.02043	-0.30883	-0.16463	0.28840
C5	0.13994	0.15933	0.26278	-0.01939	-0.10345	-0.06142	0.08406

H6	0.06391	0.19833	0.29418	-0.13442	-0.09585	-0.11514	-0.03857
H7	0.04802	0.20698	0.28852	-0.15896	-0.08154	-0.12025	-0.07742
H8	0.06602	0.18049	0.24494	-0.11447	-0.06445	-0.08946	-0.05002
H9	0.06231	0.1712	0.24728	-0.10889	-0.07608	-0.09248	-0.03281
H10	0.00784	0.2161	0.26235	-0.20826	-0.04625	-0.12726	-0.16201
H11	0.04878	0.18792	0.2412	-0.13914	-0.05328	-0.09621	-0.08586

Table 5 lists the NPA charge difference values used together with the Fukui function and dual descriptor maps. Diagram of Fukui functions is illustrated in Figure 9. The purpose of this analysis is not to assign an isolated reaction center from a single numerical sign but to identify the molecular region with the strongest local electronic response. Because atom-wise values can be sensitive to the population analysis scheme and sign convention, they should be interpreted together with the MEP and NBO results rather than as absolute reactivity constants [86,87].

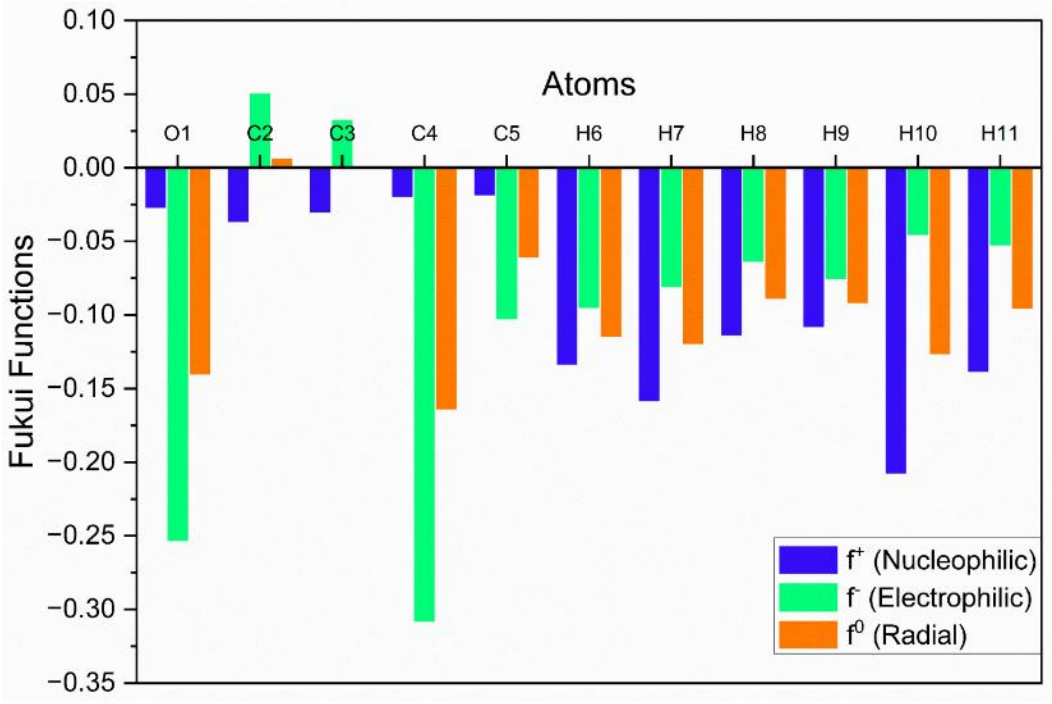


Figure 9. Fukui-function maps of 2,3-DHF, showing neutral, positive, and negative regions.

The dual-descriptor map in Figure 10, together with the numerical trends in Table 5, identifies the oxygen atom and C4=C5 unit as the dominant local-response regions of 2,3-DHF. This interpretation is consistent with the molecular electrostatic potential map, where the negative electrostatic potential is concentrated around the oxygen atom and the unsaturated region, and with the natural bond orbital result showing strong *LP(2) O1 → π(C4–C5)** donation. Therefore, the chemically meaningful conclusion is that the O1–C5=C4 enol-ether fragment is the principal reactive domain of 2,3-DHF, particularly for electrophilic addition, radical or oxidative activation, and polymerization processes. Hydrogen-centered values should be treated

cautiously because they are more sensitive to the population analysis procedure and are not interpreted here as primary reaction sites [88].

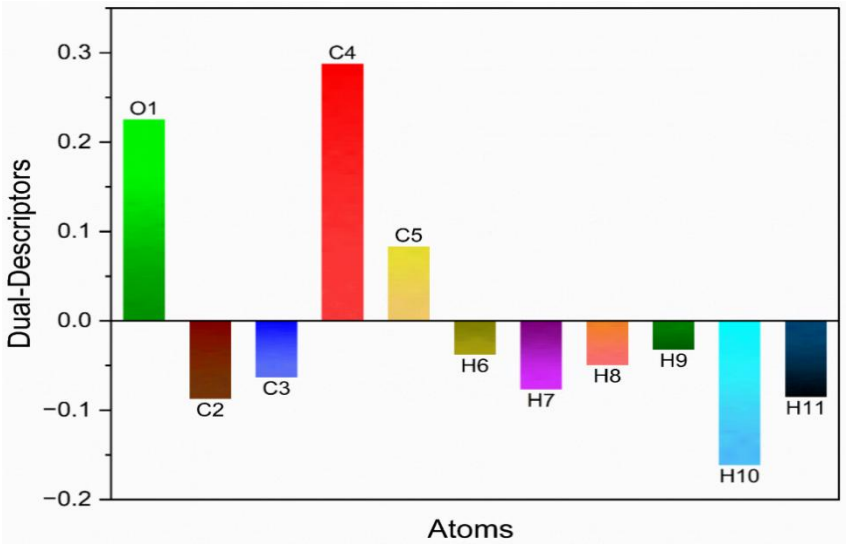


Figure 10. Dual-descriptor plot of 2,3-DHF.

Mechanistic relevance and practical application

The mechanistic relevance of the calculations becomes clearer when the FMO, GRP, MEP, NBO, Fukui function, and dual-descriptor results are considered together. The global descriptors showed that neutral 2,3-DHF has a comparatively hard electronic structure, whereas the local descriptors showed that the O1–C5=C4 enol-ether fragment remains the chemically dominant region. This distinction is important for mechanism prediction: global hardness describes the whole-molecule resistance to charge transfer, whereas the local descriptors identify where an approaching reagent is most likely to interact.

For reaction design, the results suggest that electrophiles, radical initiators, oxidants, and catalyst sites should be oriented toward the oxygen-adjacent C=C region when modeling the addition, oxidation, ring-opening, or polymer growth steps. For molecular modeling, the MEP map can guide electrostatic interaction placement, the Fukui function and dual-descriptor values can prioritize atoms for reactive-site screening, and the NBO/RDG/ELF/LOL descriptors can help verify whether a proposed intermediate or transition-state model preserves the expected oxygen-to-π delocalization and ring-strain relief. Thus, the practical value of the study is not the direct prediction of a single reaction yield but the generation of atom-level descriptors that can guide the comparative modeling of 2,3-DHF and substituted dihydrofuran scaffolds.

ELF and LOL Analysis

Electron localization function (ELF) and localized orbital locator (LOL) analyses were performed to visualize the electron localization and bonding features in real space. ELF values close to 1 indicate strongly localized electron pairs, values close to 0.5 correspond to electron-gas-like delocalization, and lower values indicate depleted or less localized regions. The LOL provides a complementary view of the localized orbital character. These analyses were performed to verify whether the real-space localization pattern supports the bonding picture obtained from the NBO and MEP analyses. Figures 11-13 present the shaded-surface and contour representations of these descriptors for the optimized structure [89,90].

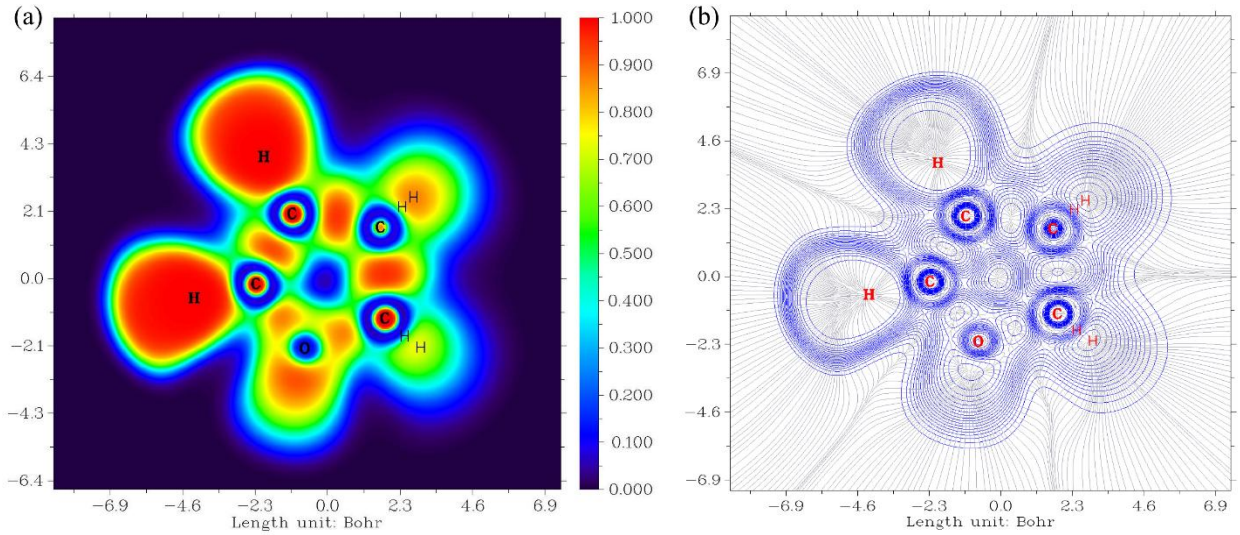


Figure 11. (a) Shaded surface map with projection and (b) contour map with projection of the electron localization function (ELF) analysis of 2,3-DHF.

The ELF map in Figure 11 highlights the localized electron density around covalent bonds and lone-pair regions, whereas lower-value regions occur between bonding domains. This pattern is consistent with localized C-H and C-O sigma bonds, together with partial electron delocalization involving the O-C4-C5 fragment [91]. Therefore, the ELF results support, rather than replace, the NBO interpretation of oxygen-assisted delocalization.

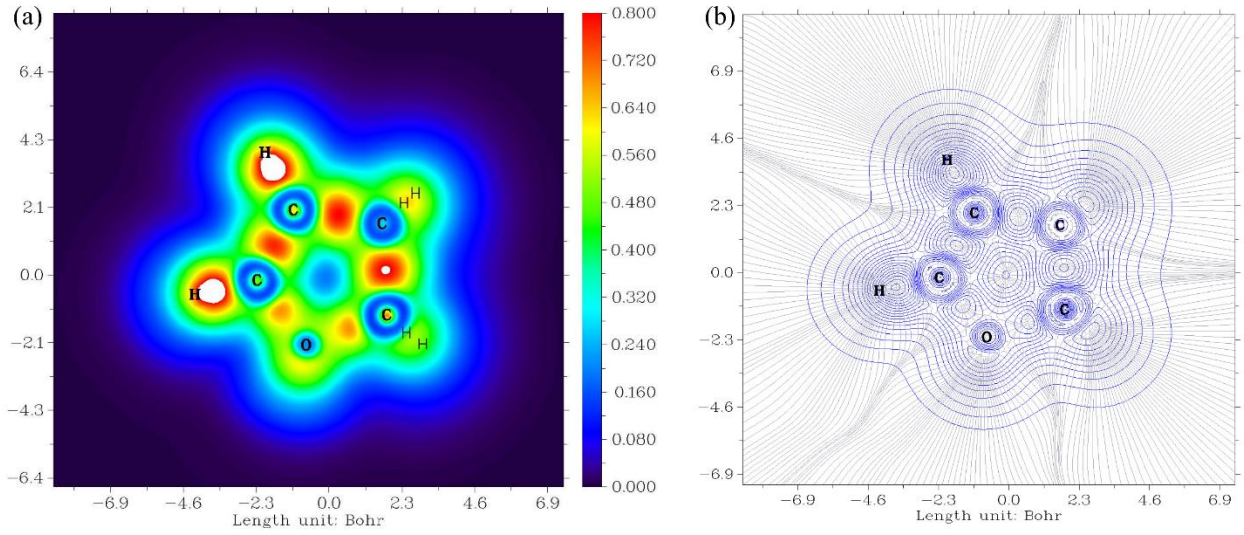


Figure 12. (a) Color-shaded map of the localized orbital locator (LOL) and (b) contour map with projection of the LOL analysis of 2,3-DHF.

The LOL map in Figure 12 provides a complementary view of orbital localization. High LOL values appear near localized bonding and core regions, whereas lower values indicate more delocalized regions of the

valence density. Together, the ELF and LOL maps support the conclusion that oxygen lone-pair donation and C=C antibonding acceptor character contribute to the electronic structure of the molecule [92].

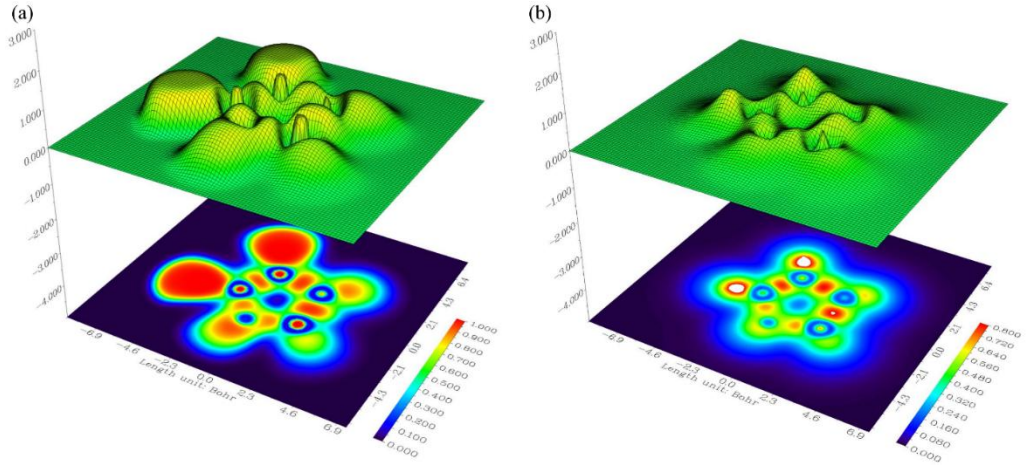


Figure 13. Three-dimensional projections of (a) ELF and (b) LOL.

Figure 13 compares the three-dimensional ELF and LOL projections of the two dimers. Localized features near hydrogen atoms and bonding regions are expected from the core and sigma-bond electron density, while the oxygen and unsaturated carbon regions show the electronic organization responsible for the main reactive domain. Therefore, these topological descriptors complement the MEP, FMO, NBO, and Fukui-function analyses by showing where the electron density is localized or delocalized in real space [93].

Physicochemical, permeability, and BOILED-Egg interpretation

SwissADME descriptors were included only to provide physicochemical and permeability-related contexts for 2,3-DHF. The values in Table 6 describe a very small molecule with a molecular weight of approximately 70 g mol^{-1}, zero rotatable bonds, one hydrogen-bond acceptor, no hydrogen-bond donor, low topological polar surface area **(**9.23 $Å^2$**)**, and moderate calculated lipophilicity, with a consensus logP of approximately 0.99. These features indicate low structural complexity and a permeability-favorable physicochemical profile, which may be useful when considering 2,3-DHF as a reactive scaffold or fragment-like starting point. However, the practical relevance of a fragment depends on experimentally validated binding, controlled reactivity, and subsequent structural optimization, rather than rule compliance alone [94–99].

The BOILED-Egg model was interpreted based on the combined effects of lipophilicity and polarity. With WLOGP = 0.92 and TPSA = 9.23 $Å^2$, 2,3-DHF falls within a region consistent with high passive gastrointestinal absorption in the model. Because the molecule is very small and weakly polar, blood–brain barrier permeation cannot be excluded using this descriptor alone. However, these predictions do not imply pharmacological usefulness, safety, target selectivity, or metabolic stability. This indicates that the size, polarity, and lipophilicity of the scaffold are compatible with passive membrane permeation [99]. Therefore, these permeability-related descriptors should be considered together with quantum-chemical results. The same oxygen-adjacent C=C region responsible for useful synthetic reactivity may also contribute to metabolic transformation, covalent reactivity, and polymerization under suitable conditions. Because cytochrome P450 inhibition, pan-assay interference behavior, toxicity, and metabolic stability outputs are not tabulated here, no definitive absorption, distribution, metabolism, excretion, toxicity, or safety claims are made. For chemical biology or medicinal chemistry applications, permeability, metabolic stability, toxicity, covalent binding tendency, and target binding would require direct experimental

validation [100,101]. Therefore, the SwissADME and BOILED-Egg discussions are used only to show how the computed electronic structure can support scaffold-level decision-making. 2,3-DHF is better viewed as a small reactive building block or fragment-like scaffold with permeability-favorable physicochemical descriptors, while its chemically active enol-ether region must be considered carefully during reaction design, molecular modeling, and any future biological assessment.

Table 6. The physicochemical, permeability-relevant, and fragment-likeness descriptors of 2,3-DHF were reported to contextualize scaffold behavior rather than direct drug candidacy.

Druglikeness Parameters	Value	Lipophilicity Parameters	Value
Rotatable bonds	0	iLOGP	1.55
H-bond acceptors	1	XLOGP3	0.80
H-bond donors	0	WLOGP	0.92
Molar refractivity	19.84	MLOGP	0.21
TPSA	9.23 Å²	SILICOS-IT LogP	1.46
Bioavailability score	0.55	Consensus LogP	0.99
Pure water solubility (ESOL)	1.17×10^{1} mg/mL	—	—
log Kp (skin permeation)	–6.16 cm/s	—	—
Lipinski rule violations	0	—	—

Conclusion

This study provides an integrated quantum-chemical description of 2,3-dihydrofuran and clarifies how a comparatively stable whole-molecule electronic structure can coexist with a strongly localized reactive region. Geometry optimization showed that the neutral structure adopted a slightly puckered five-membered ring, which helped reduce the ring strain while keeping the O1–C5=C4 enol-ether fragment electronically accessible. Frontier orbital and global reactivity analyses revealed a relatively large highest occupied molecular orbital–lowest unoccupied molecular orbital gap of 5.77 eV in the gas phase, with only small solvent-dependent changes in dimethyl sulfoxide, chloroform, and diethyl ether. This indicates that the overall electronic pattern was not strongly altered by the continuum solvent environment. The most important finding is that the global electronic hardness does not represent uniform chemical inertness in 2,3-dihydrofuran. Molecular electrostatic potential, Fukui function, dual-descriptor, and natural bond orbital results consistently identified the oxygen atom and C4=C5 unit as the dominant local-response regions. The strong LP(2) O1 → π*(C4–C5) interaction, with a stabilization energy of 28.6 kcal mol^{-1}, indicates that oxygen lone-pair donation into the C4=C5 antibonding orbital is the main electronic factor responsible for activating the enol-ether fragment. This explains why the O1–C5=C4 region is most relevant to electrophilic addition, radical or oxidative activation, ring-opening, and polymerization-related processes. Real-space analysis further supports this interpretation. Reduced density gradient analysis identified weak van der Waals contacts and steric repulsion within the ring framework, which helped rationalize the puckered geometry. Electron localization function and localized orbital locator maps show

localized σ-bond regions and oxygen-assisted delocalization around the unsaturated fragment. The combined outcome is a coherent structure–reactivity picture: 2,3-dihydrofuran is globally stabilized but locally activated at the enol ether unit. These findings provide practical atom- and bond-level descriptors for reaction site selection, mechanistic modeling, and comparison with substituted oxygen-containing heterocycles. The SwissADME and BOILED-Egg results should be treated only as physicochemical context; permeability, biological activity, toxicity, and metabolic stability require experimental validation.

Acknowledgements

The authors gratefully acknowledge the Faculty of Technology, Materials Science, and Nanotechnology Laboratory, Nepal Academy of Science and Technology (NAST), for providing the software and computational facilities.

Declaration Statements

Competing Interests
The authors declare that they have no competing interests.

Funding
This research received no specific grant from any funding agency in the public, commercial, or not-for-profit sectors.

Data Availability
The data supporting the findings of this study are available from the corresponding author upon reasonable request.

Ethics Approval
Not applicable.

Consent to Participate
Not applicable.

Consent for Publication
Not applicable.

Author contributions (Contributor Roles Taxonomy, CRediT)

Khakendra Basnet: Conceptualization, Methodology, Resource, Investigation, Software, Visualization, Writing – original draft. **Jeevan Ghimire:** Visualization, Investigation, Resource, Software. **Bhijan Neupane:** Methodology, Formal Analysis, Data Curation, Software, Visualization, Writing – original draft, Writing – review & editing, Supervision.

References

[1] García Criado, M., Myers-Smith, I.H., Bjorkman, A.D. *et al.* Plant traits poorly predict winner and loser shrub species in a warming tundra biome. *Nat Commun* **14**, 3837 (2023). https://doi.org/10.1038/s41467-023-39573-4

[2] Vengrytė, M., & Raudonė, L. (2024). Phytochemical profiling and biological activities of rhododendron subsect. ledum: discovering the medicinal potential of labrador tea species in the Northern Hemisphere. *Plants*, *13*(6), 901. https://doi.org/10.3390/plants13060901

[3] Kashanna, J., Kumar, R. A., Kishore, R., Kumar, D. N., & Kumar, A. S. (2018). 2, 3-Dihydrofurans as Potential Cytotoxic and Antibacterial Agents: Tandem Knoevenagel− Michael Cyclization for the Synthesis of 2, 3-Dihydrofurans by Using α-Tosyloxy Ketone Precursors. *Chemistry & Biodiversity*, *15*(11), e1800277. https://doi.org/10.1002/cbdv.201800277

[4] Zhao, Y., Wong, Y. C., & Yeung, Y. Y. (2015). An Unexpected 2, 3-Dihydrofuran Derivative Ring Opening Initiated by Electrophilic Bromination: Scope and Mechanistic Study. *The Journal of Organic Chemistry*, *80*(1), 453-459. https://doi.org/10.1021/jo502453f

[5] Park, S. M., Lee, Y. R., Kim, H. L., & Kwon, C. H. (2017). Conformational structures of the tetrahydrofuran cation determined using one-photon mass-analyzed threshold ionization spectroscopy. *Physical Chemistry Chemical Physics*, *19*(45), 30362-30369. https://doi.org/10.1039/C7CP05646J

[6] Xing, J., Zhu, W., Ye, B., Lu, T., Hayashi, T., & Dou, X. (2020). Rhodium-catalyzed diverse arylation of 2, 5-dihydrofuran: controllable divergent synthesis via four pathways. *ACS Catalysis*, *10*(5), 2958-2963. https://doi.org/10.1021/acscatal.0c00265

[7] Cheng, S., Tang, S., Tsona, N. T., & Du, L. (2017). The influence of the position of the double bond and ring size on the stability of hydrogen bonded complexes. *Scientific reports*, *7*(1), 11310. https://doi.org/10.1038/s41598-017-11921-7

[8] Hernández-Fernández, J., Puello-Polo, E., & Marquez, E. (2023). Experimental–Density Functional Theory (DFT) Study of the Inhibitory Effect of Furan Residues in the Ziegler–Natta Catalyst during Polypropylene Synthesis. *International journal of molecular sciences*, *24*(18), 14368. https://doi.org/10.3390/ijms241814368

[9] An, T., Ryu, H., & Choi, T. L. (2023). Living Alternating Ring-Opening Metathesis Copolymerization of 2, 3-Dihydrofuran to Provide Completely Degradable Polymers. *Angewandte Chemie International Edition*, *62*(47), e202309632. https://doi.org/10.1002/anie.202309632

[10] Alwe, H. D., Sharma, A., Walavalkar, M. P., Dhanya, S., & Naik, P. D. (2015). Formation of Furan along with HO2 during the OH-Initiated Oxidation of 2, 5-DHF and 2, 3-DHF: An Experimental and Computational Study. *The Journal of Physical Chemistry A*, *119*(12), 2793-2801. https://doi.org/10.1021/jp5122454

[11] Matsubara, M., Osada, F., Nakajima, M., Imai, T., Nishimura, K., Oyama, T., & Tsukiyama, K. (2016). Isomerization and dissociation of 2, 3-dihydrofuran (2, 3-DHF) induced by infrared free electron laser. *Journal of Photochemistry and Photobiology A: Chemistry*, *322*, 53-59. https://doi.org/10.1016/j.jphotochem.2016.02.014

[12] Mozafari, M., Brodovitch, J. C., Chandrasena, L., & Percival, P. W. (2016). Characterization of free radicals in clathrate hydrates of furan, 2, 3-dihydrofuran, and 2, 5-dihydrofuran by muon spin spectroscopy. *The Journal of Physical Chemistry A*, *120*(43), 8521-8528. https://doi.org/10.1021/acs.jpca.6b08653

[13] Guđmundsson, A., Gustafson, K. P., Mai, B. K., Yang, B., Himo, F., & Backvall, J. E. (2018). Efficient formation of 2, 3-dihydrofurans via iron-catalyzed cycloisomerization of α-allenols. *ACS Catalysis*, *8*(1), 12-16. https://doi.org/10.1021/acscatal.7b03515

[14] Wu, Y., Xu, N., Yang, M., Liu, Y., Tang, C., & Huang, Z. (2020). Ignition delay time measurement and kinetic modeling of furan, and comparative studies of 2, 3-dihydrofuran and tetrahydrofuran at low to intermediate temperatures by using a rapid compression machine. *Combustion and Flame*, *213*, 226-236. https://doi.org/10.1016/j.combustflame.2019.12.010

[15] Salnikov, O. G., Kovtunova, L. M., Skovpin, I. V., Bukhtiyarov, V. I., Kovtunov, K. V., & Koptyug, I. V. (2018). Mechanistic Insight into the Heterogeneous Hydrogenation of Furan Derivatives with the use of Parahydrogen. *ChemCatChem*, *10*(5), 1178-1183. https://doi.org/10.1002/cctc.201701653

[16] Schalk, O., Geng, T., Hansson, T., & Thomas, R. D. (2018). The ring-opening channel and the influence of Rydberg states on the excited state dynamics of furan and its derivatives. *The Journal of Chemical Physics*, *149*(8). https://doi.org/10.1063/1.5024655

[17] Kanhounnon, W. G., Kuevi, U. A., Kpotin, G. A., Koudjina, S., Houngue, A. K., Atohoun, G. Y., ... & Badawi, M. (2019). Quantum mechanistic study of furan and 2-methylfuran hydrodeoxygenation on molybdenum and tungsten sulfide clusters. *Journal of Molecular Modeling*, *25*(8), 237. https://doi.org/10.1007/s00894-019-4086-4

[18] Röder, A., de Oliveira, N., Grollau, F., Mestdagh, J. M., Gallician, G., Gaveau, M. A., ... & Briant, M. (2020). High-resolution vacuum ultraviolet absorption spectra of 2, 3-and 2, 5-dihydrofuran. *The Journal of Chemical Physics*, *153*(13). https://doi.org/10.1063/5.0015835

[19] Guerra Faura, G., Nguyen, T., & France, S. (2021). Catalyst-Controlled Chemodivergent Reactions of 2-Pyrrolyl-α-diazo-β-ketoesters and Enol Ethers: Synthesis of 1, 2-Dihydrofuran Acetals and Highly Substituted Indoles. *The Journal of Organic Chemistry*, *86*(15), 10088-10104. https://doi.org/10.1021/acs.joc.1c00826

[20] Choi, K., & Hong, S. H. (2023). Chemically recyclable oxygen-protective polymers developed by ring-opening metathesis homopolymerization of cyclohexene derivatives. *Chem*, *9*(9), 2637-2654. http://doi.org/10.1016/j.chempr.2023.05.038

[21] M.J. Frisch, and more than 10, Gaussian Inc.: Wallingford, CT, USA, 2009.

[22] Dennington, R. D. I. I., Keith, T. A., & Millam, J. M. (2016). *GaussView, Version 6.0.16*. Semichem Inc., Shawnee Mission, KS.

[23] van Leeuwen, R. (1994). *Kohn-Sham potentials in density functional theory*. Amsterdam, The Netherlands: Vrije Universiteit.

[24] Bickelhaupt, F. M., & Baerends, E. J. (2000). Kohn-Sham density functional theory: predicting and understanding chemistry. *Reviews in computational chemistry*, 1-86. https://doi.org/10.1002/9780470125922

[25] Lee, C., Yang, W., & Parr, R. G. (1988). Development of the Colle-Salvetti correlation-energy formula into a functional of the electron density. *Physical review B*, *37*(2), 785. https://doi.org/10.1103/PhysRevB.37.785

[26] Becke, A. D. (1993). Density-functional thermochemistry. III. The role of exact exchange. *The Journal of chemical physics*, *98*(7), 5648-5652. https://doi.org/10.1063/1.464913

[27] Chiacchio, M. A., & Legnani, L. (2024). Density functional theory calculations: A useful tool to investigate mechanisms of 1, 3-dipolar cycloaddition reactions. *International Journal of Molecular Sciences*, *25*(2), 1298. https://doi.org/10.3390/ijms25021298

[28] Marenich, A. V., Cramer, C. J., & Truhlar, D. G. (2009). Universal solvation model based on solute electron density and on a continuum model of the solvent defined by the bulk dielectric constant and atomic surface tensions. *The Journal of Physical Chemistry B*, *113*(18), 6378-6396. https://doi.org/10.1021/jp810292n

[29] Koopmans, T. (1934). Über die Zuordnung von Wellenfunktionen und Eigenwerten zu den einzelnen Elektronen eines Atoms. *physica*, *1*(1-6), 104-113. https://doi.org/10.1016/S0031-8914(34)90011-2

[30] Cortés Arriagada, D. (2013). Global and local reactivity indexes applied to understand the chemistry of graphene oxide and doped graphene. *Journal of molecular modeling*, *19*, 919-930. https://doi.org/10.1007/s00894-012-1642-6

[31] Rajesh, S., Gunasekaran, S., & Rajesh, P. (2018). HOMO-LUMO, NBO and Vibrational analysis of Sitagliptin by using DFT calculations and Experimental Study (FT-IR, FT-Raman and UV-Visible Spectroscopies). *Int. J. Chem Tech. Res*, *11*, 107-122. http://dx.doi.org/10.20902/IJCTR.2018.110714

[32] Ojha, J. K., Ramesh, G., & Reddy, B. V. (2023). Structure, chemical reactivity, NBO, MEP analysis and thermodynamic parameters of pentamethyl benzene using DFT study. *Chemical Physics Impact*, *7*, 100280. https://doi.org/10.1016/j.chphi.2023.100280

[33] Sakr, M. A., Sherbiny, F. F., & El-Etrawy, A. A. S. (2022). Hydrazone-based materials; DFT, TD-DFT, NBO analysis, fukui function, MESP analysis, and solar cell applications. *Journal of Fluorescence*, *32*(5), 1857-1871. https://doi.org/10.1007/s10895-022-03000-6

[34] Huo, E., Shahab, S., Al Saud, S., Cheng, W., Lu, P., Sheikhi, M., ... & Kaviani, S. (2021). Quantum chemical modeling, synthesis, spectroscopic (FT-IR, excited States, UV–Vis) studies, FMO, QTAIM, NBO and NLO analyses of two new azo derivatives. *Journal of Molecular Structure*, *1243*, 130810. https://doi.org/10.1016/j.molstruc.2021.130810

[35] Sauer, M., Hofkens, J., & Enderlein, J. (2011). Basic principles of fluorescence spectroscopy. *Handbook of fluorescence spectroscopy and imaging*, *1*, 30. https://doi.org/10.1007/978-3-319-26788-3_4

[36] Rocha, F. S., Gomes, A. J., Lunardi, C. N., Kaliaguine, S., & Patience, G. S. (2018). Experimental methods in chemical engineering: Ultraviolet visible spectroscopy—UV-Vis. *The Canadian Journal of Chemical Engineering*, *96*(12), 2512-2517. https://doi.org/10.1002/cjce.23344

[37] Mekoung, P. M. A., Malloum, A., Govindarajan, M., Mballa, R. N., Patouossa, I., Zintchem, A. A. A., ... & Mbouombouo, I. N. (2023). Spectroscopic properties (FT-IR, NMR and UV) and DFT studies of amodiaquine. *Heliyon*, *9*(12). http://doi.org/10.1016/j.heliyon.2023.e22187

[38] Guégan, F., Merzoud, L., Chermette, H., & Morell, C. (2021). A Perspective on the So-Called Dual Descriptor. *Chemical Reactivity in Confined Systems: Theory, Modelling and Applications*, 99-112. https://doi.org/10.1002/9781119683353.ch6

[39] Lu, T., & Chen, F. (2012). *Journal of Computational Chemistry, 33*(5), 580. https://doi.org/10.1002/jcc.22885

[40] Humphrey, W., Dalke, A., & Schulten, K. (1996). VMD: Visual Molecular Dynamics. *Journal of Molecular Graphics, 14*(1), 33-38. https://doi.org/10.1016/0263-7855(96)00018-5

[41] Akman, F., Demirpolat, A., Kazachenko, A. S., Kazachenko, A. S., Issaoui, N., & Al-Dossary, O. (2023). Molecular structure, electronic properties, reactivity (ELF, LOL, and Fukui), and NCI-RDG studies of the binary mixture of water and essential oil of Phlomis bruguieri. *Molecules*, *28*(6), 2684. https://doi.org/10.3390/molecules28062684

[42] Savin, A., Nesper, R., Wengert, S., & Fässler, T. F. (1997). ELF: The electron localization function. *Angewandte Chemie International Edition in English*, *36*(17), 1808-1832. https://doi.org/10.1002/anie.199718081

[43] Trivedi, R., Banerjee, A., & Bandyopadhyay, D. (2021). Study of electronic structure, stabilities and electron localization behavior of AgPbn (n= 1–14) nanoclusters: a first principal investigation. *Physica E: Low-dimensional Systems and Nanostructures*, *131*, 114725. https://doi.org/10.1016/j.physe.2021.114725

[44] Isravel, A. D., Jeyaraj, J. K., Thangasamy, S., & John, W. J. (2021). DFT, NBO, HOMO-LUMO, NCI, stability, Fukui function and hole–Electron analyses of tolcapone. *Computational and Theoretical Chemistry*, *1202*, 113296. https://doi.org/10.1016/j.comptc.2021.113296

[45] Jacobsen, H. (2008). Localized-orbital locator (LOL) profiles of chemical bonding. *Canadian Journal of Chemistry*, *86*(7), 695-702. https://doi.org/10.1139/v08-052

[46] Fernandes, H. S., Cerqueira, N. M., Sousa, S. F., & Melo, A. (2022). A molecular mechanics energy partitioning software for biomolecular systems. *Molecules*, *27*(17), 5524. https://doi.org/10.3390/molecules27175524

[47] Verkhovtsev, A. V., Solov'yov, I. A., & Solov'yov, A. V. (2022). Structure and Dynamics of Bio- and Macromolecules. In *Dynamics of Systems on the Nanoscale* (pp. 137-199). Cham: Springer International Publishing. https://doi.org/10.1007/978-3-030-99291-0_4

[48] Tegegn, D. F., Belachew, H. Z., & Salau, A. O. (2024). DFT/TDDFT calculations of geometry optimization, electronic structure and spectral properties of clevudine and telbivudine for treatment of chronic hepatitis B. *Scientific Reports*, *14*(1), 8146. https://doi.org/10.1038/s41598-024-58599-2

[49] Wang, L., Xie, F., Wang, D., Sun, D., & Wu, M. (2025). First-principles investigation on the atomic-level mechanism of acetic acid corrosion on carbon steel. *npj Materials Degradation*, *9*(1), 99. https://doi.org/10.1038/s41529-025-00643-1

[50] Jin, X., Zhou, J., Wang, S., & Hu, B. (2016). Computational study on structure and properties of new energetic material 3, 7-bis (dinitromethylene)-2, 4, 6, 8-tetranitro-2, 4, 6, 8-tetraaza-bicyclo [3.3. 0] octane. *Química Nova*, *39*(4), 467-473. https://doi.org/10.5935/0100-4042.20160054

[51] Renj, D. L., Geetha, R. R. J., Benifa, A., Amalanathan, M., Mary, M. S. M., Ratković, Z., ... & Micheal, J. (2024). Density functional theory calculations, vibrational spectral analysis and topological analysis of 1-acethyl-2 (4-isopropoxy-3-methoxyphenyl) cyclopropane with docking studies. *Chemical Physics Impact*, *8*, 100524. https://doi.org/10.1016/j.chphi.2024.100524

[52] Choudhary, V., Bhatt, A., Dash, D., & Sharma, N. (2019). DFT calculations on molecular structures, HOMO–LUMO study, reactivity descriptors and spectral analyses of newly synthesized diorganotin (IV) 2-chloridophenylacetohydroxamate complexes. *Journal of computational chemistry*, *40*(27), 2354-2363. https://doi.org/10.1002/jcc.26012

[53] Omar, S., Shkir, M., Khan, M. A., Ahmad, Z., & AlFaify, S. (2020). A comprehensive study on molecular geometry, optical, HOMO-LUMO, and nonlinear properties of 1, 3-diphenyl-2-propen-1-ones chalcone and its derivatives for optoelectronic applications: a computational approach. *Optik*, *204*, 164172. https://doi.org/10.1016/j.ijleo.2020.164172

[54] Etminan, N., Yoosefian, M., Raissi, H., & Hakimi, M. (2016). Solvent effects on the stability and the electronic properties of histidine/Pd-doped single-walled carbon nanotube biosensor. *Journal of Molecular Liquids*, *214*, 313-318. https://doi.org/10.1016/j.molliq.2015.12.009

[55] Mohamed, A., Visco Jr, D. P., Breimaier, K., & Bastidas, D. M. (2025). Effect of molecular structure on the B3LYP-computed HOMO–LUMO gap: a structure− property relationship using atomic signatures. *ACS omega*, *10*(3), 2799-2808. https://doi.org/10.1021/acsomega.4c08626

[56] Xu, Y., Chu, Q., Chen, D., & Fuentes, A. (2021). HOMO–LUMO gaps and molecular structures of polycyclic aromatic hydrocarbons in soot formation. *Frontiers in Mechanical Engineering*, *7*, 744001. https://doi.org/10.3389/fmech.2021.744001

[57] Moreno-Ceballos, A., Castro, M. E., Caballero, N. A., Mammino, L., & Melendez, F. J. (2024). Implicit and explicit solvent effects on the global reactivity and the density topological parameters of the preferred conformers of caespitate. *Computation*, *12*(1), 5. https://doi.org/10.3390/computation12010005

[58] Ekoro, I. A., Mbonu, J. I., Ogwuche, C. E., Agu, S. C., & Bawa, H. A. (2025). Theoretical investigation of solvent effects on reactivity, spectroscopic properties, and inhibitory potential of a dihydropyridine derivative against Vibrio cholorae: DFT, molecular docking and pharmacokinetics evaluation. *Discover Chemistry*, *2*(1), 116. https://doi.org/10.1007/s44371-025-00189-w

[59] Miar, M., Shiroudi, A., Pourshamsian, K., Oliaey, A. R., & Hatamjafari, F. (2021). Theoretical investigations on the HOMO–LUMO gap and global reactivity descriptor studies, natural bond orbital, and nucleus-independent chemical shifts analyses of 3-phenylbenzo [d] thiazole-2 (3 H)-imine and its

para-substituted derivatives: Solvent and substituent effects. *Journal of Chemical Research*, *45*(1-2), 147-158. https://doi.org/10.1177/1747519820932091

[60] Omrani, R., Zouaghi, M. O., & Arfaoui, Y. (2020). Mechanistic density functional theory study of the Claisen Rearrangement Diels-Alder Cycloaddition domino sequence for the synthesis of the caged garcinia xanthone. *Journal of Molecular Structure*, *1202*, 127305. https://doi.org/10.1016/j.molstruc.2019.127305

[61] Hazarika, R., & Kalita, B. (2021). Elucidating the therapeutic activity of selective curcumin analogues: DFT-based reactivity analysis. *Structural Chemistry*, *32*(4), 1701-1715. https://doi.org/10.1007/s11224-021-01745-7

[62] Omer, R., Ahmed, L., Koparır, P., & Hama, J. (2022). Impact of Solvent Polarity on the molecular properties of Dimetridazole. *El-Cezeri*, *9*(2), 740-747. https://doi.org/10.31202/ecjse.1000757

[63] Isravel, A. D., Jeyaraj, J. K., Thangasamy, S., & John, W. J. (2021). DFT, NBO, HOMO-LUMO, NCI, stability, Fukui function and hole–Electron analyses of tolcapone. *Computational and Theoretical Chemistry*, *1202*, 113296. https://doi.org/10.1016/j.comptc.2021.113296

[64] Shafiq, I., Raza, N., Dildar, S., & Bullo, S. (2025). Unraveling the NLO potential of isoquinoline functionalized chromophores via molecular modeling using DFT/TD-DFT approaches. *Scientific Reports*, *15*(1), 23236. https://doi.org/10.1038/s41598-025-04911-7

[65] Rahuman, M. H., Muthu, S., Raajaraman, B. R., Raja, M., & Umamahesvari, H. (2020). Investigations on 2-(4-Cyanophenylamino) acetic acid by FT-IR, FT-Raman, NMR and UV-Vis spectroscopy, DFT (NBO, HOMO-LUMO, MEP and Fukui function) and molecular docking studies. *Heliyon*, *6*(9). http://doi.org/10.1016/j.heliyon.2020.e04976

[66] Briceño-Vargas, F. M., Quesadas-Rojas, M., Mirón-López, G., Cáceres-Castillo, D., Carballo, R. M., Mena-Rejón, G. J., & Quijano-Quiñones, R. F. (2023). Molecular orbital and topological electron density study of n→ π* interactions: amides and thioamides cases. *RSC advances*, *13*(45), 31321-31329. https://doi.org/10.1039/D3RA06038A

[67] Eşme, A. S. L. I., & Sağdınç, S. G. (2017). Spectroscopic (FT–IR, FT–Raman, UV–Vis) analysis, conformational, HOMO-LUMO, NBO and NLO calculations on monomeric and dimeric structures of 4–pyridazinecarboxylic acid by HF and DFT methods. *Journal of Molecular Structure*, *1147*, 322-334. https://doi.org/10.1016/j.molstruc.2017.06.110

[68] Jawaria, R., Hussain, M., Khalid, M., Khan, M. U., Tahir, M. N., Naseer, M. M., ... & Shafiq, Z. (2019). Synthesis, crystal structure analysis, spectral characterization and nonlinear optical exploration of potent thiosemicarbazones based compounds: A DFT refine experimental study. *Inorganica Chimica Acta*, *486*, 162-171. https://doi.org/10.1016/j.ica.2018.10.035

[69] Hajam, T. A., Saleem, H., Syed Ali Padhusha, M., & Mohammed Ameen, K. K. (2022). Quantum mechanical study, spectroscopic (FT-IR, FT-Raman and UV-Vis) study, NBO, NLO analysis and molecular docking studies of 2-ethoxy-4-(pyridine-2yliminomethyl)-phenol. *Polycyclic Aromatic Compounds*, *42*(7), 4819-4842. https://doi.org/10.1080/10406638.2021.1896561

[70] Sakthivel, S., Alagesan, T., Muthu, S., Abraham, C. S., & Geetha, E. (2018). Quantum mechanical, spectroscopic study (FT-IR and FT-Raman), NBO analysis, HOMO-LUMO, first order hyperpolarizability and docking studies of a non-steroidal anti-inflammatory compound. *Journal of Molecular Structure*, *1156*, 645-656. https://doi.org/10.1016/j.molstruc.2017.12.024

[71] Martynov, A. G., Mack, J., May, A. K., Nyokong, T., Gorbunova, Y. G., & Tsivadze, A. Y. (2019). Methodological survey of simplified TD-DFT methods for fast and accurate interpretation of UV–Vis–NIR spectra of phthalocyanines. *ACS omega*, *4*(4), 7265-7284. https://doi.org/10.1021/acsomega.8b03500

[72] Shivaleela, B., & Hanagodimath, S. M. (2020). UV-visible spectra, HOMO-LUMO studies on Coumarin derivative using Gaussian Software. In *Conference proceedings of one day online international conference on advanced materials*.

[73] Yang, J. W., Choi, J. K., Kim, M. C., & Kim, H. (2019). A study of UV–vis spectroscopic and DFT calculation of the UV absorber in different solvent. *Progress in Organic Coatings*, *135*, 168-175. https://doi.org/10.1016/j.porgcoat.2019.05.034

[74] Mohammed, M. H., Ajeel, F. N., & Khudhair, A. M. (2017). Adsorption of gas molecules on graphene nanoflakes and its implication as a gas nanosensor by DFT investigations. *Chinese journal of physics*, *55*(4), 1576-1582. https://doi.org/10.1016/j.cjph.2017.05.013

[75] Saeed, F., Idrees, N., & Imran, M. (2025). DFT based structural modeling of chemotherapy drugs via topological indices and curvilinear regression. *Scientific Reports*, *15*(1), 33755. https://doi.org/10.1038/s41598-025-97982-5

[76] Shokuhi Rad, A., Esfahanian, M., Maleki, S., & Gharati, G. (2016). Application of carbon nanostructures toward SO2 and SO3 adsorption: a comparison between pristine graphene and N-doped graphene by DFT calculations. *Journal of Sulfur Chemistry*, *37*(2), 176-188. https://doi.org/10.1080/17415993.2015.1116536

[77] Magar, B. S., Pudasainee, K., Pandey, P., Neupane, M. K., Lamichhane, R. R., Gurung, B., ... & Adhikari, B. (2025). Theoretical investigation on PD-L1-In-1 for cancer immunotherapy via density functional theory. *Scientific Reports*, *15*(1), 30476. https://doi.org/10.1038/s41598-025-92180-9

[78] Kebiroglu, M. H., & Ak, F. Investigation of Optimized Density of States (DOS) Analysis, UV-Visible Spectroscopy, NMR Spectroscopy, and Molecular Electrostatic Potential (MEP) Mapping of Ru-486 and Its Derivatives. Afyon Kocatepe Üniversitesi Fen Ve Mühendislik Bilimleri Dergisi, 25(6), 1279-1290. https://doi.org/10.35414/akufemubid.1537900

[79] Boursas, F., Berrah, F., Kanagathara, N., Anbalagan, G., & Bouacida, S. (2019). XRD, FT-IR, FT-Raman spectra and ab initio HF vibrational analysis of bis (5-amino-3-carboxy-1H-1, 2, 4-triazol-4-ium) selenate dihydrate. *Journal of Molecular Structure*, *1180*, 532-541. https://doi.org/10.1016/j.molstruc.2018.12.037

[80] Kumar, A., Pandey, A., & Mishra, A. (2020). Computational study of novel 2, 3-bis [(1-methyl-1H-imidazole-2-yl) sulfanyl] quinoxaline: Structural aspects, spectroscopi c investigation, HOMO-LUMO, MESP, NLO, ADMET predictions, and molecula r docking studies as potential biotin carboxylase and antibiotics resistan t aminoglycoside phosphotransferase aph (2'') IVA enzyme inhibitor. *Asian J. Chem*, *32*, 706-726. https://doi.org/10.14233/ajchem.2020.22507

[81] Ganiev, B., Mardonov, U., & Kholikova, G. (2023). Molecular structure, HOMO-LUMO, MEP-–Analysis of triazine compounds using DFT (B3LYP) calculations. *Materials Today: Proceedings*. https://doi.org/10.1016/j.matpr.2023.09.191

[82] Basha, F., Khan, F. L. A., Muthu, S., & Raja, M. (2021). Computational evaluation on molecular structure (Monomer, Dimer), RDG, ELF, electronic (HOMO-LUMO, MEP) properties, and spectroscopic profiling of 8-Quinolinesulfonamide with molecular docking studies. *Computational and Theoretical Chemistry*, *1198*, 113169. https://doi.org/10.1016/j.comptc.2021.113169

[83] Shanmugapriya, N., Balachandran, V., Revathi, B., Narayana, B., Salian, V. V., Vanasundari, K., & Sivakumar, C. (2021). Quantum chemical calculation, performance of selective antimicrobial activity using molecular docking analysis, RDG and experimental (FT-IR, FT-Raman) investigation of 4-[{2-[3-(4-chlorophenyl)-5-(4-propan-2-yl) phenyl)-4, 5-dihydro-1H-pyrazol-1-yl]-4-oxo-1, 3-thiazol-5 (4H)-ylidene} methyl] benzonitrile. *Heliyon*, *7*(7). http://doi.org/10.1016/j.heliyon.2021.e07634

[84] Manickavelu, T., Govindrajan, B., Sambantham, M., Panneerselvam, P., & Irfan, A. (2022). Computational investigation, effects of polar and non-polar solvents on optimized structure with

topological parameters (ELF, LOL, AIM, and RDG) of three glycine derivative compounds. *Structural Chemistry*, *33*(4), 1295-1319. https://doi.org/10.1007/s11224-022-01930-2

[85] Lefi, N., Kazachenko, A. S., Raja, M., Issaoui, N., & Kazachenko, A. S. (2023). Molecular structure, spectral analysis, molecular docking and physicochemical studies of 3-bromo-2-hydroxypyridine monomer and dimer as bromodomain inhibitors. *Molecules*, *28*(6), 2669. https://doi.org/10.3390/molecules28062669

[86] Zamora, P. P., Bieger, K., Cuchillo, A., Tello, A., & Muena, J. P. (2021). Theoretical determination of a reaction intermediate: Fukui function analysis, dual reactivity descriptor and activation energy. *Journal of Molecular Structure*, *1227*, 129369. https://doi.org/10.1016/j.molstruc.2020.129369

[87] Sevvanthi, S., Muthu, S., Raja, M., Aayisha, S., & Janani, S. P. E. S. (2020). PES, molecular structure, spectroscopic (FT-IR, FT-Raman), electronic (UV-Vis, HOMO-LUMO), quantum chemical and biological (docking) studies on a potent membrane permeable inhibitor: dibenzoxepine derivative. *Heliyon*, *6*(8). https://doi.org/10.1016/j.heliyon.2020.e04724

[88] Sánchez-Márquez, J. (2019). New advances in conceptual-DFT: an alternative way to calculate the Fukui function and dual descriptor. *Journal of Molecular Modeling*, *25*(5), 123.https://doi.org/10.1007/s00894-019-4000-0

[89] Arulaabaranam, K., Muthu, S., Mani, G., & Geoffrey, A. B. (2021). Speculative assessment, molecular composition, PDOS, topology exploration (ELF, LOL, RDG), ligand-protein interactions, on 5-bromo-3-nitropyridine-2-carbonitrile. *Heliyon*, *7*(5). http://doi.org/10.1016/j.heliyon.2021.e07061

[90] Sheena Mary, Y., Shyma Mary, Y., Serdaroglu, G., Kaya, S., Sarojini, B. K., Umamahesvari, H., & Mohan, B. J. (2022). Conformational analysis, spectroscopic insights, chemical descriptors, ELF, LOL and molecular docking studies of potential pyrimidine derivative with biological activities. *Polycyclic Aromatic Compounds*, *42*(8), 5160-5170. https://doi.org/10.1080/10406638.2021.1924803

[91] Abisha, W., Dhas, D. A., Balachandran, S., & Joe, I. H. (2023). Molecular structure, spectroscopic elucidation (FT-IR, FT-Raman, UV-Visible and NMR) with NBO, ELF, LOL, RDG, Fukui, drug likeness and molecular docking analysis on dimethomorph. *Polycyclic Aromatic Compounds*, *43*(5), 3988-4031. https://doi.org/10.1080/10406638.2022.2083195

[92] Awad, M. K., Halim, W. A., Atlam, F. M., & Fawzy, M. M. (2025). A multiscale computational investigation for protection of carbon steel surface by pyrazolo-pyrimidine derivatives. *Scientific Reports*, *15*(1), 32576. https://doi.org/10.1038/s41598-025-19022-6

[93] Hammoudan, I., Aboulmouhajir, A., Dakir, M., Temsamani, D. R., Bakhouch, M., Bazi, D. E., & Chtita, S. (2023). Mechanistic elucidation of Diels–Alder cycloaddition reactions between quinoflavonoid and substituted butadiene using LOL, ELF, QTAIM, and DFT studies. *Structural Chemistry*, *34*(3), 959-969. https://doi.org/10.1007/s11224-022-02058-z

[94] Khedkar, N. R., Sindkhedkar, M., & Joseph, A. (2025). Fragment-based drug discovery: Small fragments, big impact− Success stories of approved oncology therapeutics. *Bioorganic Chemistry*, 108197. https://doi.org/10.1016/j.bioorg.2025.108197

[95] Daina, A., & Zoete, V. (2016). A boiled-egg to predict gastrointestinal absorption and brain penetration of small molecules. *ChemMedChem*, *11*(11), 1117-1121. https://doi.org/10.1002/cmdc.201600182

[96] Chedik, L., Mias-Lucquin, D., Bruyere, A., & Fardel, O. (2017). In silico prediction for intestinal absorption and brain penetration of chemical pesticides in humans. *International Journal of Environmental Research and Public Health*, *14*(7), 708. https://doi.org/10.3390/ijerph14070708

[97] Khedkar, N. R., Sindkhedkar, M., & Joseph, A. (2025b). Fragment-Based Drug Discovery: Small Fragments, Big Impact − Success stories of approved Oncology Therapeutics. Bioorganic Chemistry, 156, 108197. https://doi.org/10.1016/j.bioorg.2025.108197

[98] AlKharboush, D. F., Kozielski, F., Wells, G., & Porta, E. O. (2025). Fragment-based drug discovery: A graphical review. Current Research in Pharmacology and Drug Discovery, 9, 100233. https://doi.org/10.1016/j.crphar.2025.100233

[99] Miebs, G., Mielniczuk, A., Kadziński, M., & Bachorz, R. A. (2024). Beyond the arbitrariness of Drug-Likeness Rules: rough set theory and decision rules in the service of drug design. Applied Sciences, 14(21), 9966. https://doi.org/10.3390/app14219966

[100] Baell, J., & Walters, M. A. (2014b). Chemistry: Chemical con artists foil drug discovery. Nature, 513(7519), 481–483. https://doi.org/10.1038/513481a

[101] Tanoli, Z., Schulman, A., & Aittokallio, T. (2024b). Validation guidelines for drug-target prediction methods. Expert Opinion on Drug Discovery, 20(1), 31–45. https://doi.org/10.1080/17460441.2024.2430955